

## Spatial and functional arrangement of Ebola virus polymerase inside phase-separated viral factories

Jingru Fang<sup>1,2</sup>, Guillaume Castillon<sup>3,4</sup>, Sebastien Phan<sup>4</sup>, Sara McArdle<sup>1</sup>, Chitra Hariharan<sup>1</sup>, Mark H. Ellisman<sup>4</sup>, Ashok A. Deniz<sup>2</sup>, Erica Ollmann Saphire<sup>1,\*</sup>

<sup>1</sup>La Jolla Institute for Immunology, La Jolla, CA, USA, <sup>2</sup>Scripps Research, La Jolla, CA, USA, <sup>3</sup>CMM Electron Microscopy Core facility, University of California San Diego, La Jolla, CA, USA, <sup>4</sup>National Center for Microscopy and Imaging Research, Center for Research in Biological Systems, University of California San Diego, La Jolla, CA, USA.

\*Corresponding author (erica@lji.org)

### Abstract

Ebola virus (EBOV) infection induces formation of membrane-less, cytoplasmic compartments termed viral factories, in which multiple viral proteins gather and from which diverse viral biogenesis arises. Key to viral factory function is recruitment of the EBOV polymerase, a multifunctional machine that mediates replication and expression of the viral RNA genome. Here we show that intracellularly reconstituted EBOV viral factories are biomolecular condensates, with composition-dependent internal dynamics of exchange that likely facilitates viral replication. We report that EBOV viral factories display either droplet-like or network-like morphology, which could be influenced by multivalent intermolecular interactions between viral proteins. Within the viral factory, we found EBOV polymerase is not uniformly distributed, but instead clusters into foci. The distance between these foci increases when viral replication is enabled. This unique view of EBOV propagation suggests a form-to-function relationship that describes how physical properties and internal structures of biomolecular condensates influence and regulate viral biogenesis.

### Introduction

Viruses are architects of cellular remodeling needed to fulfill life-cycle events inside host cells. Some viruses remodel host cells by inducing formation of nonequilibrium, membrane-less compartments, also termed inclusion bodies or viral factories (VFs), that separate essential viral replication and assembly events from other cellular processes<sup>1-11</sup>. As exemplified by many known cellular membrane-less organelles, such as the multiphasic nucleolus<sup>12</sup>, different interdependent cellular processes can be spatially separated into distinct co-existing phases inside the membrane-less compartment. In contrast, how multiple interdependent viral biogenesis steps are coordinated inside viral factories remains unclear.

Among viruses that induce VF formation, many are non-segmented, negative-strand RNA viruses (nNSVs)<sup>2,3,5-8,10,11</sup>. The negative sense RNA genome of nNSVs is coated by oligomerized viral nucleoprotein to form a helical RNP structure. During viral biogenesis, the viral polymerase transcribes the negative-strand RNA genome (termed vRNA) into multiple mRNAs encoding individual viral genes that are translated by host cell ribosomes into viral proteins. Meanwhile, the same viral polymerase must also coordinate synthesis of a complementary, positive-strand of the viral genome, termed cRNA, which acts as a template to replicate progeny negative-strand vRNAs. As cRNA and vRNA are produced, both are immediately coated with the viral nucleoprotein to form helical cRNP and vRNP (ribonucleoprotein) assemblies, respectively. However, only vRNP, which is linked to viral polymerase, is assembled into progeny virions<sup>13</sup>. The occurrence of these different virus biogenesis reactions inside VFs and the presence of different species of viral RNAs with different functions and different fates likely requires some spatial regulation.

51 Recent studies indicated that several nNSV VFs are biomolecular condensates that have  
52 viscoelastic material properties, including VFs derived from vesicular stomatitis, rabies, measles  
53 viruses, and human metapneumovirus<sup>11,14-17</sup>. The importance and potential biological relevance  
54 of these viscoelastic properties was highlighted by inhibition of RSV infection in an animal model  
55 by a condensate-hardening drug<sup>18</sup>.

56 Formation of biomolecular condensates follows basic principles of phase separation wherein  
57 molecules separate from a well-mixed system into multiple phases with distinct constituents, at  
58 different concentrations in each phase<sup>19,20</sup>. This phase separation in biological systems is driven  
59 by multivalent intermolecular interactions, based on the intrinsic properties of the protein and RNA  
60 constituents<sup>21-24</sup>, and is further influenced by other features of the system's free energy  
61 landscape<sup>25,26</sup>, which include kinetic effects such as the macroscopic segregation of dynamically  
62 asymmetric mixtures<sup>27</sup>. Under physiological conditions, the concentration of key constituents  
63 essentially controls the state of intracellular phase separation, which can be approximated in a  
64 phase diagram<sup>19</sup>. This theoretical framework can offer mechanistic and quantitative insights into  
65 VF condensate dynamics from which biological functions arise or are enabled. Deciphering phase  
66 behaviors of intracellular VF condensates, and the spatial localization of the steps of virus  
67 biogenesis within them, will outline the form-to-function relationship of VFs and enhance our  
68 understanding of nNSV replication.

69 Among nNSVs, Ebola virus is a zoonotic, human pathogen that causes near-annual outbreaks  
70 of disease with up to 90% mortality (WHO<sup>28</sup>, CDC<sup>29</sup>). The only FDA-approved vaccine for Ebola  
71 virus protects against only Ebola virus Zaire (EBOV), but not against the other species, including  
72 the Sudan ebolavirus linked to an outbreak of disease that began in Uganda in 2022. Further,  
73 therapeutic antibodies approved thus far are also specific for EBOV and may poorly penetrate  
74 immune-privileged sites where Ebola virus can lurk. Additional therapeutic strategies are needed,  
75 and will be accelerated by a better understanding of essential and conserved intracellular events  
76 in Ebola virus replication.

77 Here, we sought to define how EBOV VFs spatially accommodate and control viral RNA  
78 synthesis with an emphasis on the organization of the EBOV polymerase complex within VFs. To  
79 dissect the individual contribution of viral elements to VF organization and dynamics, we took a  
80 bottom-up approach to reconstitute EBOV VFs within cells beginning with minimal viral protein  
81 components and viral minigenome reporter RNA. We determined that intracellularly reconstituted  
82 EBOV VFs exist as biomolecular condensates that have reduced internal dynamics upon  
83 recruitment of EBOV polymerase. Although EBOV VFs typically have a droplet-shape, we  
84 described an additional, network-like morphology of EBOV VFs. Using advanced confocal  
85 microscopy, we found an unexpected punctate distribution pattern of EBOV polymerase inside  
86 droplet-like VFs and that this distribution of EBOV polymerase links to polymerase-mediated viral  
87 RNA synthesis. Leveraging thin-section electron microscopy (EM) and multi-tilt electron  
88 tomography (ET), we further resolved several foci of EBOV polymerase at invaginated or  
89 interconnected boundary of the network-like VF, surrounded by helical vRNP-like structures.  
90 Collectively, these multi-scale imaging approaches provide an unprecedented view of the spatial  
91 organization by which Ebola virus orchestrates multiple biogenesis steps and deploys viral  
92 replication machinery inside viral factories.

93

## 94 **Results**

### 95 **1. Engineering of a fluorescence protein-tagged EBOV VP35 for live cell imaging of** 96 **EBOV viral factories (VFs)**

97 Intracellular EBOV VFs are found to undergo fusion during infection<sup>6</sup>. This observation served  
98 as the first hint that EBOV VFs could be biomolecular condensates. Thus, we undertook a  
99 quantitative approach to determine whether EBOV VFs are indeed fluid condensates rather than  
100 solid aggregates and define the internal molecular dynamics within EBOV VFs. Since microscopy  
101 of live, EBOV-infected cells under BSL4 containment is neither feasible nor amenable to

102 controlling VF composition, we first established a transfection-based, live-cell system to perform  
103 fluorescence recovery after photobleaching (FRAP) analysis with intracellularly reconstituted  
104 EBOV VFs.

105 To monitor EBOV VF with live-cell imaging, we adapted an approach used to image VFs in  
106 live cells infected with Rabies (RABV)<sup>15</sup>. We fused an EBOV VF constituent, the polymerase  
107 cofactor VP35, to an N-terminal HA epitope tag and a fluorescent protein, mNeonGreen (mNG)  
108 to generate HA-mNG-VP35. We confirmed that HA-mNG-VP35 protein expresses at a similar  
109 level as the wild-type (VP35-WT), and retains sufficient ability to act as the polymerase cofactor  
110 that supports EBOV viral RNA synthesis (**Supplementary Figure 1a**).

111 VP35 interacts with EBOV nucleoprotein (NP) and chaperones the NP monomer (NP<sup>0</sup>) prior  
112 to NP oligomerization<sup>30</sup>. As a polymerase cofactor, VP35 bridges the EBOV large polymerase  
113 protein (L) to NP-coated viral genomic material<sup>31</sup>. Since these multivalent intermolecular  
114 interactions VP35 involved in might provide the foundation for biomolecule phase separation, we  
115 first confirmed that the mNG tag did not affect these interactions. We performed HA-  
116 immunoprecipitation (IP) using cells co-expressing NP and L with either mNG-HA-VP35, HA-  
117 VP35 (positive control), or mNG-HA (negative control). In the presence of NP alone or with NP  
118 and L, HA-VP35 and HA-mNG-VP35 both immunoprecipitated with NP and L (**Figure 1a**).  
119 Immunofluorescence microscopy showed that the intracellular localization of HA-mNG-VP35  
120 resembles that of VP35-WT, when co-expressed with NP and L (**Supplementary Figure 1b**).  
121 Together, our results indicate that HA-mNG-VP35 preserves sufficient polymerase-cofactor  
122 function and fully retains interactions with NP and L for use in live-cell imaging.

## 123 **2. Reconstituted EBOV VFs display composition-dependent, viscoelastic properties in** 124 **live cells**

125 To quantitatively measure the internal mobility of EBOV VF components in a cellular context,  
126 we performed FRAP in HEK 293T cells co-transfected with EBOV NP and HA-mNG-VP35. Both  
127 NP and VP35 proteins contain multiple disordered and low complexity regions (**Figure 1b**), bind  
128 RNA<sup>32,33</sup> and self-oligomerize<sup>34-37</sup>, which are common features associated with many known  
129 cellular proteins to be involved in phase separation<sup>19</sup>. Here we used NP and VP35 as the minimal  
130 components to reconstitute EBOV VFs.

131 Reconstituted EBOV VFs had diameters ranging from sub-micrometer to 10  $\mu\text{m}$   
132 (**Supplementary Figure 1c**). Because the high mobility of sub- $\mu\text{m}$  VF makes it challenging to  
133 accurately measure fluorescence recovery within achievable microscopy frame-rate, we focused  
134 on medium-sized VFs (4-5  $\mu\text{m}$  diameter). We photobleached a 1  $\mu\text{m}$  diameter center spot in the  
135 VFs and monitored the fluorescence recovery of the bleached spot until the system returned to  
136 equilibrium. To quantify the kinetics of fluorescence recovery from which we can extract  
137 parameter values that describe the timescale of the fast vs. slow diffusion event and the fraction  
138 of immobile molecules, we fitted double-normalized fluorescence intensity values from the  
139 moment of photobleaching until equilibrium was reached to a two-phase association model  
140 (**Methods**).

141 As a control, HA-mNG-VP35 expressed alone formed gel-like, dense phases in the cytoplasm  
142 (**Figure 1c**). Most cells have large quantities of sub- $\mu\text{m}$  VP35-condensates with high apparent  
143 mobility relative to the dilute phase, but a small number of VP35-condensates had a larger size  
144 suitable for FRAP. These large condensates have multiple dark internal regions that lacked  
145 fluorescence. After photobleaching a center spot of VP35 condensates, we observed only partial  
146 fluorescence recovery (**Figure 1f**, green curve). This slower recovery rate could be due to a non-  
147 diffusion based binding reaction like that which occurs with VP35 self-oligomerization or RNA  
148 binding, since diffusion of a similar-sized protein occurs within milliseconds for similar-sized  
149 regions<sup>38</sup>.

150 We next evaluated reconstituted EBOV VFs via co-expression of HA-mNG-VP35 and NP. The  
151 combination of HA-mNG-VP35 and NP yielded homogenous binary condensates (**Figure 1d**) that

152 appeared to be fluid-like based on frequently observed fusions between condensates or fission  
153 of one condensate into two parts (**Supplementary Figure 2a**), and on non-fluorescence objects  
154 trafficking through VFs (**Supplementary Figure 2b**). Over half the transfected cells had easily  
155 identifiable  $>5\mu\text{m}$  condensates. Fluorescence recovery inside VP35-NP condensates is highly  
156 dynamic with faster molecular exchange than that measured in VP35-alone condensate (**Figure**  
157 **1f**, red vs. green curves). This faster recovery likely reflects contributions of VP35-NP interactions.  
158 In VP35-NP condensates, 84.6% of VP35 molecules (with a 95% CI [83.89%,85.90%]) are mobile,  
159 while in VP35-alone condensates,  $<50\%$  of VP35 are mobile. Moreover, the half-time of the fast  
160 association phase ( $t_{1/2\text{FAST}}$ ) for VP35-NP condensates was  $\sim 5.5$  s, which is consistent with that  
161 reported for VFs in RABV-infected cells<sup>15</sup> ( $t_{1/2\text{FAST}} \sim 5.2$  s), and the half time for the slow association  
162 phase ( $t_{1/2\text{SLOW}}$ ) was  $\sim 21.5$  s (**Figure 1f**).

163 Co-expression of mNG-HA-VP35 with NP and EBOV large polymerase protein (L) resulted in  
164 dense phases in the cytoplasm that contained all three proteins (**Supplementary Figure 1b**).  
165 VP35 and NP had homogenous distribution in these dense ternary condensates, but whether the  
166 distribution of L was also homogeneous was unclear (**Figure 1e**). In VP35-NP-L condensates,  
167 78% of mNG-HA-VP35 (with a 95% CI [77.7%,78.4%]) are mobile (**Figure 1f**, blue curve), which  
168 is on average 7% lower than VP35+NP, suggesting that VP35-L interactions may immobilize a  
169 small population of VP35. In both binary and ternary condensates, bleach-pulses induced loss of  
170 fluorescence signal was around 12% of the prebleach signal at equilibrium, which justifies the  
171 comparison of VP35-mobile fraction in both condensates (**Supplementary Figure 2c**). Further,  
172 the similar  $t_{1/2\text{FAST}}$  and  $t_{1/2\text{SLOW}}$  values for binary and ternary condensates likely indicates similar  
173 molecular interactions mediate VP35 mobility, although the percentage of fast association events  
174 fell from 80.3% to 64.3% (**Figure 1f**). This reduction suggests that L affects the stoichiometry of  
175 different molecular interactions involving VP35.

176 Our FRAP results quantitatively showed that EBOV VFs reconstituted with NP and VP35  
177 display composition-dependent, viscoelastic behaviors in live cells. The addition of L immobilizes  
178 a small, but detectable, fraction of VP35 inside the reconstituted VFs.

### 179 **3. Intracellular localization analysis of FLAG-tagged EBOV large polymerase protein L** 180 **with confocal fluorescence microscopy**

181 We next assessed whether EBOV L is immobilized in a specific location within VFs using  
182 immunofluorescence microscopy. To facilitate detection of L, we engineered recombinant L with  
183 an N-terminal 2xFLAG tag (FLAG-L) as previously described<sup>39</sup> since the only currently available  
184 L polyclonal antibody can non-specifically bind to proteins other than EBOV L (**Supplementary**  
185 **Figure 1d**).

186 First, we co-expressed NP, VP35 and FLAG-L in HEK 293T cells and labeled EBOV VFs  
187 using a monoclonal antibody targeting NP. Although NP was present throughout EBOV VFs, NP  
188 molecules at the VF periphery were immunolabeled more efficiently than the NP inside VF,  
189 leading to an “empty” droplet-like morphology of EBOV VFs, which was previously described<sup>40,41</sup>.  
190 Unexpectedly, FLAG-L was not homogeneously distributed within reconstituted VFs and had a  
191 different staining pattern than NP (**Figure 2a**). Instead, FLAG-L clustered into networks  
192 comprising interconnected foci within the ternary condensate, suggesting that an intrinsic property  
193 of L drives a different phase behavior than VP35 or NP.

194 To link this phase behavior of EBOV L to its biological function, we further analyzed L  
195 localization in the presence of an active RNA substrate for L, the EBOV minigenome, which allows  
196 reconstitution of L-mediated MG replication and transcription. The EBOV minigenome we used  
197 here is bicistronic (2cis-MG), which contains two reporter genes encoding GFP (for imaging) and  
198 *Renilla* luciferase (for quantification) in a tandem cassette carrying authentic EBOV gene start-  
199 and end signals. EBOV regulatory sequences, the 3' leader and 5' trailer, required for replication,  
200 transcription and encapsidation of viral RNAs<sup>42</sup>, flank the bicistronic cassette. Using the  
201 replication-competent version of the 2cis-MG (**Figure 2b**, Rep-comp. MG), we confirmed that the

202 L construct, FLAG-L, we engineered is competent to fulfill its biological function as it retained 74%  
203 of the wildtype L (L-WT) activity (**Figure 2c**).

204 In GFP+ cells having successful reconstitution of EBOV MG replication and transcription,  
205 FLAG-L still clustered into networks of interconnected foci inside VFs (**Figure 2d**). Besides, in  
206 fixed cells, GFP reporter signals were preferentially trapped in both VFs and nucleoli, which both  
207 have features of biomolecular condensates.

208 We next asked whether modulating viral RNA synthesis affects EBOV L organization inside  
209 VFs. Since adding or removing MG system elements could affect the overall valency of protein-  
210 protein/RNA interactions or the molecular composition inside EBOV VFs, we incorporated a  
211 previously characterized mutation into the 5' trailer of the EBOV 2cis-MG that allows transcription  
212 but disables vRNA replication<sup>43</sup>. Reporter activity measured in this replication-deficient MG (Rep-  
213 def. MG) system reflects only viral transcription (**Figure 2b**, Rep-def. MG). With Rep-def. MG,  
214 FLAG-L retained 33% of the L-WT activity, indicating that the 2xFLAG tag may have affected L-  
215 mediated transcription (**Figure 2c**). Nevertheless, with FLAG-L, when replication was disabled,  
216 the L foci inside EBOV VFs were more closely spaced compared to that seen for replication-  
217 competent VFs (**Figure 2e, f**). This different spacing is unlikely to be associated with the  
218 expression levels since FLAG-L was expressed at equivalent levels in the Rep-comp. and Rep-  
219 def. MG systems (**Figure 2c**). Together, our results revealed a unique localization pattern of  
220 EBOV polymerase L inside VF and established a potential link between the spatial distribution of  
221 L within the VF and viral RNA synthesis events mediated by L.

#### 222 **4. Network-like VFs exist in EBOV-GFP-ΔVP30 infected cells**

223 Among the EBOV VFs reconstituted with the transcription and replication of EBOV MG in  
224 transfected HEK 293T cells, some display a granular, network-like morphology instead of the  
225 typical droplet-like morphology (**Figure 3a**). We thus examined whether network-like VFs also  
226 occur during virus infection.

227 To characterize VF morphology in EBOV-infected cells, we used the biologically contained  
228 EBOV-GFP-ΔVP30 virus, which is morphologically indistinguishable from wild-type EBOV, but  
229 approved for use in BSL2+ containment<sup>44</sup>. In this system, a GFP gene replaces the gene encoding  
230 the viral transcription factor, VP30, so that EBOV-GFP-ΔVP30 virus can grow only in cell lines  
231 stably expressing VP30. Here, Vero cells stably expressing EBOV VP30 (Vero-VP30) were  
232 infected with EBOV-GFP-ΔVP30 in a synchronized manner and the cells were fixed and  
233 inactivated at 18 hours post-infection, when the VF size is comparable to that in HEK 293T cells  
234 transfected with the EBOV MG system<sup>45</sup>. We then used immunofluorescence-labeled NP as a  
235 marker to detect VFs in GFP-positive (i.e., EBOV-GFP-ΔVP30 infected) Vero-VP30 cells.

236 EBOV-GFP-ΔVP30 infected cells had either droplet-like or network-like VFs (**Figure 3b**), with  
237 the majority (77%) had droplet-like VFs and a stronger immunofluorescence staining of NP at the  
238 VF periphery as previously reported<sup>45</sup>. The remaining 23% of infected cells harbored network-like  
239 VFs, which, in contrast to droplet-like VFs located at discrete sites in the cytoplasm, occupied a  
240 more extended region that included a group of small VFs either interconnected or separated by  
241 only a small distance. Our results suggested that the both droplet-like and network-like  
242 morphology of EBOV VFs exist during EBOV infection.

#### 243 **5. Engineering a split-APEX2 tag for electron microscopy analyses of EBOV polymerase 244 L-VP35 complexes**

245 To dissect the spatial organization of EBOV polymerase inside VFs at nanometer resolution,  
246 we used APEX2, a peroxidase tag engineered to indicate the location of tagged proteins in  
247 electron microscopy (EM) imaging. Specifically, we used the split-APEX2 (sAPEX) system<sup>46</sup>,  
248 consisting of two inactive fragments, sAP and sEX. We genetically fused the small fragment sEX  
249 to L (L-sEX) and the large fragment sAP, along with a V5 epitope tag, to VP35 (VP35-V5-sAP)

250 **(Figure 4a)**. Interaction of L with VP35 during the formation of an active EBOV polymerase  
251 complex joins the sAP and sEX fragments to reconstitute APEX2 peroxidase activity.

252 We confirmed that sAPEX-tagged EBOV polymerase is functionally active **(Figure 4b)**, using  
253 a Pol1-based, monocistronic EBOV minigenome (Pol1-MG) system<sup>47</sup> that works similarly to the  
254 T7-based, bicistronic EBOV MG, but contains a single gene encoding the firefly luciferase reporter  
255 **(Figure 4c)**. VP35-V5-sAP expression levels were significantly higher than the V5-tagged VP35  
256 control (VP35-V5). L-sEX was also expressed to higher levels than wild type L, which could  
257 explain the correspondingly higher MG activity seen for sAPEX2-tagged EBOV polymerase  
258 **(Figure 4d)**.

259 In cells transfected with sAPEX2-tagged EBOV polymerase and the Pol1-MG system, we  
260 confirmed a site-specific reconstitution of sAPEX2 activity, as evidenced by APEX2-mediated  
261 conversion of a fluorogenic substrate at sites marked with VP35-V5-sAP immunofluorescence.

262 We noted that VP35-V5-sAP formed a network-like dense phase, whereas VP35-V5 formed  
263 droplet-like dense phases **(Figure 4e)**, upper panel). These two morphologies of VP35-dense  
264 phase in transfected HEK293T cells are comparable to those we observed with EBOV VF in virus-  
265 infected Vero-VP30 cells. Further, the two morphologies resemble possible outcomes of phase  
266 separation occurring via nucleation-growth vs. spinodal decomposition<sup>26,48</sup>. In regions in the  
267 phase diagram that correspond to a thermodynamically metastable state, a new phase as in a  
268 small spherical “nucleus” can stochastically form and grow in size via intermolecular interactions.  
269 Meanwhile, in regions that correspond to an unstable initial state, small fluctuations in composition  
270 or density (i.e., increased concentration of one constituent) could translate into ripples in the  
271 systems’ free energy landscape, such that phase separation occurs spontaneously and features  
272 in a network-like domain morphology that can be made persistent by kinetic arrest. The range of  
273 intermolecular interactions underlining the dense vs. dilute phase controls the condensate  
274 morphology<sup>21,49</sup>.

275 The atypical network-like morphology of VP35-V5-sAP could be attributed to increased  
276 valence of the inter-molecular interaction in the sAPEX2-tagged L-VP35 complex, since trans-  
277 complementation of the sAPEX-tag creates an additional intermolecular interaction between L  
278 and VP35 **(Figure 4e)**, lower panel). To test this possibility independently of sAPEX2-tagging, we  
279 increased the valence of inter-molecular interactions that involve VP35 by adding EBOV VP24,  
280 an EBOV protein which also interacts with VP35<sup>50</sup>. Upon co-expression of VP24 with VP35-V5  
281 and the Pol1-MG system components, VP35-V5 droplets were replaced by the network-like VP35-  
282 V5 dense phase that colocalized with VP24 **(Figure 4f)**, upper panel). This result could indicate  
283 that increased valence of intermolecular interactions indeed alters VP35 phase behavior.  
284 However, even in the presence of VP24, which is present during virus infection, the sAPEX2-  
285 tagged EBOV L-VP35 complex remained in the network-like dense phase **(Figure 4f)**, lower panel).

286 In summary, we successfully engineered an intracellularly active EBOV polymerase carrying  
287 a split-APEX2 tag that will allow localization of EBOV polymerase in electron microscopy (EM)  
288 analyses. Although the split-APEX2 tag did affect the intracellular localization pattern of VP35 in  
289 cells reconstituted with the EBOV MG system, this altered VP35 pattern is likely not completely  
290 artificial, since the same VP35 localization pattern occurred upon co-expression of EBOV VP24,  
291 an EBOV protein present during natural EBOV infection. The altered VP35 pattern also coincides  
292 with the network-like morphology of EBOV VF we also observed in EBOV-GFP-ΔVP30-infected  
293 cells **(Figure 3b)**. Therefore, we next carried out EM analysis on the localization of sAPEX2-  
294 tagged EBOV polymerase in cells reconstituted with the Pol1-based EBOV MG system.

## 295 **6. Nanoscale localization of split-APEX2-tagged EBOV polymerase complex with thin-** 296 **section transmission electron microscopy (thin-section TEM)**

297 We used the sAPEX2 tag engineered into the L-VP35 complex, to locate the EBOV  
298 polymerase within the compact cellular contents revealed by EM. Upon staining with 3,3’-  
299 diaminobenzidine (DAB), trans-complementation of sAPEX2 catalyzes DAB polymerization with

300 minimal diffusion. The resulting DAB polymers alone at the site of active APEX2 are chromogenic,  
301 which can be detected by light microscopy (LM). Further, DAB polymers are osmiophilic, and thus  
302 capture osmium upon OsO<sub>4</sub> staining to increase electron density associated with DAB deposits  
303 (**Figure 5a**). OsO<sub>4</sub> also stains unsaturated lipids<sup>51</sup> and reacts with nucleic acids<sup>52,53</sup> to outline  
304 cellular architecture in a specimen.

305 After optimization of transfection and staining conditions, we could detect sAPEX2-specific  
306 DAB deposits in bright field light microscopy images of HEK 293T cells transfected with sAPEX2-  
307 tagged EBOV polymerase together with other Pol1-MG components. DAB darkening was  
308 intensified after osmification and DAB-positive (DAB+) cells were readily recognizable in resin-  
309 embedded samples under light microscopy, which facilitates production of 70 nm thin-sections  
310 containing a DAB+ cell and its detection with transmission electron microscopy (TEM) (**Figure**  
311 **5b**). We observed within the same DAB+ cell network-like, electron-dense regions in cytoplasmic  
312 areas that likely correspond to EBOV VFs (**Figure 5c, Supplementary Figure 3a**). These  
313 electron-dense regions were present in cells transfected with the Pol1-MG system but not in  
314 untransfected control cells (**Supplementary Figure 3b, c**). In the DAB+ cell, EBOV-specific  
315 electron-dense regions were decorated with darker dots arranged in a pattern that correlated with  
316 the shape of DAB darkening in light microscopy (**Figure 5c, arrows**), suggesting that the locations  
317 of these darker dots in the electron micrograph corresponded to sites where sAPEX2-tagged  
318 EBOV polymerases localize.

319 In the same thin-section, we also identified cells that had no DAB staining under light  
320 microscopy (DAB-) (**Figure 5b**). These DAB- cells had the same transfection conditions as DAB+  
321 cells but sAPEX2 activity was not reconstituted. DAB- cells exhibited network-like, electron-dense  
322 VFs in the cytoplasm, similar to DAB+ cells (**Figure 5d**). By comparing the morphology of EBOV  
323 VF in DAB+ and DAB- cells, the darker dots that associate with electron-dense VF in the DAB+  
324 cell in fact indicate locations of sAPEX2-tagged EBOV polymerase (**Figure 5e**).

325 Our thin-section TEM observation revealed that sAPEX2-tagged EBOV polymerase non-  
326 uniformly localizes to the periphery of network-like VFs. In several sites in the cytoplasm, sAPEX2-  
327 tagged EBOV polymerase preferentially clusters at the junction of interconnected VFs.  
328 Surrounding the electron-dense VFs were wire-like fragments that frequently associated with  
329 neighboring VFs (**Figure 5c, d**).

### 330 **7. 3D visualization of EBOV VFs and sAPEX2-tagged polymerase by electron tomography**

331 To visualize the three-dimensional (3D) ultrastructure of EBOV VFs and elucidate the spatial  
332 distribution of the sAPEX2-tagged polymerase complex, we applied a four-tilt electron  
333 tomography (ET) collection scheme and reconstructed tomograms of subcellular volumes  
334 containing EBOV VFs and sAPEX2-tagged polymerase. Similar to thin-section TEM specimens,  
335 we transfected HEK 293T cells with the Pol1-based EBOV MG system containing sAPEX2-tagged  
336 polymerase, except we generated 200-250 nm-thick sections from subcellular regions containing  
337 DAB+ cells. Thin-section TEM allowed visualization of averaged 2D projection of all cellular  
338 content across the thin-section specimen, but multi-tilt electron tomography allowed us to resolve  
339 individual tomographic slices of the reconstructed volume with finer details of cellular matter  
340 (**Figure 6a**). To understand the cellular surroundings of EBOV VF, we manually annotated a  
341 representative tomogram at an organelle level (**Figure 6b**). Similar to previous EM analysis of  
342 virus-infected cells<sup>3,54</sup>, reconstituted EBOV VFs appeared as electron-dense clusters that lack  
343 membrane boundaries themselves, but are in close proximity to membrane-bound cellular  
344 organelles including mitochondria, the endoplasmic reticulum, the nuclear envelope and vesicles.  
345 In addition to the membrane-bound organelles, the EBOV VFs and granularities in the cytosolic  
346 surroundings were clearly resolved in the tomographic slices.

347 Across the tomographic slices, darker-stained patches near the edge of several electron-  
348 dense VFs were apparent. By mapping these darker patches in the tomogram, we reconstructed  
349 the 3D footprints of sAPEX2-tagged EBOV polymerase on a group of network-like VFs that were

350 in close proximity or even interconnected (**Figure 6b**). In the reconstructed tomograms the wire-  
351 like fragments observed in thin-section TEM appeared to be continuous filaments having random  
352 orientations. We then selected a region of interest from the whole tomogram, and performed a  
353 finer manual segmentation focusing on smaller objects surrounding the VFs (**Figure 6c**).  
354 sAPEX2-tagged EBOV polymerase appeared to dock at certain spots on the VF periphery.  
355 Ribosomes were located outside, but adjacent to EBOV VFs. We observed several loosely coiled  
356 structures either emerging from or passing through neighboring VFs, which likely gave rise to the  
357 rough surface of the VFs and are the major component of VFs (**Figure 6d**). We propose that  
358 these loosely coiled structures are the viral ribonucleoprotein complex (vRNP), which has at its  
359 core helical viral genomic RNA bound to NP<sup>55,56</sup>. The helical structure is sufficiently relaxed to  
360 allow the viral polymerase to slide along the genome during RNA synthesis. We saw no  
361 condensed vRNP in our sample, likely because VP24, which has an inhibitory effect on vRNA  
362 synthesis and can condense vRNP, was not included in the MG system<sup>57,58</sup>.

363 In a selected region from the whole tomogram, two loose-coil structures can, in fact, be traced  
364 back from their different branching sites to one parental loose coil (**Figure 6e**). One possible  
365 explanation for these interconnected coils is that viral genomic RNA associates with active  
366 transcription products. For several better-resolved loose coils in our tomogram, the coil terminus  
367 often had a small loop linked to a solid globular structure. The identity of this terminal loop and  
368 globular structure remains to be determined. In another selected region, several sAPEX2-tagged  
369 EBOV spots were identified by manually tracing the darker stained patches on an invaginated  
370 edge of electron-dense VFs. These darker-stained patches localized to the apical sides of  
371 neighboring VFs where they formed a zipper-like structure (**Figure 6f**). In reconstructed  
372 tomograms, the only obvious cellular structures that have direct contact with EBOV VFs are the  
373 single-membrane vesicles (**Figure 6 b, f**).

## 374 Discussion

375 Ebola virus (EBOV) induces formation of viral factories (VFs) in host cells that allow physical  
376 separation of viral biogenesis from other cellular processes. In this study we sought to understand  
377 the mechanisms by which EBOV VFs spatially accommodate and control viral RNA synthesis,  
378 with a particular focus on the localization of the EBOV polymerase complexes within VFs.

379 The internal dynamics we measured using FRAP for EBOV VFs produced in transfected cells  
380 are strikingly comparable to those reported for VFs in rabies virus-infected cells<sup>15</sup>. Even though  
381 the stoichiometry of transfected viral proteins cannot fully recapitulate that of virus infection, our  
382 results demonstrate the validity of using transfection-based, intracellularly reconstituted VF to  
383 study viscoelastic properties of VF in living cells.

384 The contribution of individual VF components to the internal molecular exchange within VFs  
385 was poorly characterized in previous studies. Here, we used transfection-based VF reconstitution  
386 and supplied individual EBOV components for stepwise assembly of intracellular VF. Our key  
387 finding is a notable reduction in the molecular exchange rate within EBOV VFs upon recruitment  
388 of L to the NP-VP35 binary condensate, which is likely due to interaction of L with a fraction of  
389 mobile VP35. Reducing the internal molecular exchange rate within EBOV VF could functionally  
390 impact viral RNA synthesis. Longer dwell times of EBOV polymerase and its cofactors inside VFs  
391 may facilitate the initiation step of EBOV polymerase-mediated viral RNA synthesis. A slower  
392 internal molecular exchange rate within EBOV VFs may also facilitate concurrent NP-  
393 encapsidation of nascent v/cRNA. We additionally observed that VP35 expressed in the absence  
394 of NP tends to form immobile aggregates, which indirectly supports a crucial role for NP as a  
395 scaffold for VF condensates. Given that the EBOV NP protein is 3-times bigger than VP35, the  
396 dynamic behavior of soluble NP<sup>0</sup>-VP35 complex<sup>30</sup> likely drives the mobility of VP35 in the NP-  
397 bound state regardless of other molecular interactions VP35 is involved in. The same approach  
398 we used here can be used to measure the contribution of other EBOV proteins, especially VP30,



399 to the internal dynamics within VFs and to characterize composition-dependent mobility of VFs  
400 induced by other viruses.

401 Little was previously known about the functional localization of nNSV polymerases inside cells.  
402 The lack of specific antibodies suitable for immunofluorescence labeling and the low protein  
403 abundance of viral polymerase in infected cells has made imaging of nNSV polymerases  
404 particularly challenging. An early study first identified that mCherry-tagged EBOV L polymerase  
405 homogenously locates inside VFs during infection<sup>6</sup>. Despite the value of mCherry for live-cell  
406 imaging, the activity of L-mCherry was only 10% that of unmodified L and the integrity of the L-  
407 mCherry was unclear due to the lack of a detection antibody against L at the time of the study. In  
408 contrast to insertion of a larger fluorescence protein, L protein can tolerate a small epitope tag  
409 without substantial loss of RNA synthesis activity<sup>59</sup>. A recent study using super-resolution light  
410 microscopy examined the intracellular localization of FLAG-tagged RSV L in RSV-infected cells<sup>60</sup>.  
411 In that study, RSV L concentrated non-uniformly at several sites inside RSV VFs. This result  
412 aligns well with our confocal microscopy findings that FLAG-tagged EBOV L formed foci inside  
413 VFs in cells reconstituted with the replication and expression of EBOV minigenome. A  
414 recombinant EBOV expressing FLAG-tagged L should be generated to further validate our  
415 findings with L localization in cells infected with authentic virus under BSL4 containment.

416 Beyond elucidating the functional localization of EBOV polymerase L, our work for the first  
417 time links the localization pattern of EBOV L to particular types of L-mediated viral RNA synthesis.  
418 We hypothesized that VFs have distinct sub-compartments that are dedicated to viral replication  
419 or transcription. To dissect the EBOV L localization specific to replication or transcription, we  
420 uncoupled L-mediated replication from transcription by generating a replication-deficient EBOV  
421 minigenome (MG)<sup>43</sup>. We observed an intriguing difference in EBOV L localization in cells  
422 reconstituted with replication-competent vs. replication-deficient MG systems. When viral  
423 replication was active, the foci containing L were more widely spaced than when replication was  
424 switched off. A wider spacing of L-foci could allow more NP to permeate and become available  
425 for c/vRNA encapsidation, as reduced NP availability impairs viral genome replication<sup>61</sup>.  
426 Conversely, a narrower spacing of L-foci may reflect a switch from replication to transcription,  
427 which produces flexible viral mRNAs that are less bulky, or may represent the waning activity of  
428 overall viral RNA synthesis. Our result implies that, rather than having distinct sub-compartments  
429 specialized for viral replication and transcription, the spatial organization of EBOV L expands and  
430 contracts according to the type or activity of ongoing viral RNA synthesis.

431 In addition to the spatial-functional dynamics with EBOV polymerase, we revealed an atypical,  
432 network-like morphology of EBOV VFs. In previous microscopy studies with virus-infected cells,  
433 nNSV VFs, including those induced by EBOV, appear mostly as droplet-like structures<sup>6-8,62</sup>. We  
434 did observe droplet-like VFs in EBOV-GFP-ΔVP30 infected cells, but a quarter of the cells  
435 contained network-like VFs. Interestingly, some network-like EBOV VFs had similar shapes to  
436 those observed in Marburg virus-infected cells<sup>3</sup>. The identification of both spherical and network-  
437 like VFs in EBOV-infected cells suggests that the underlying mechanisms for EBOV VF phase  
438 separation could include both nucleation-and-growth and spinodal decomposition<sup>26,48</sup>. Formation  
439 of the network-like VFs could also be an outcome of viscoelastic phase separation of dynamically  
440 asymmetric mixture<sup>27</sup>, since we observed different viscoelastic behaviors in compositionally  
441 distinct VF mixtures. Alternatively, the network-like VF could be driven by the formation of  
442 extensive RNA-RNA interactions<sup>63</sup> that involve nascent viral RNAs or cellular RNAs. Future  
443 experiments should identify the molecular basis of network-like EBOV VFs and elucidate the  
444 biological role of such atypical VFs in virus infections.

445 Finally, we visualized the precise 3D localization of EBOV polymerase with nanometer  
446 resolution in a subcellular volume using electron-tomography. Here EBOV polymerase with the  
447 APEX2 EM-tag allowed localization of the polymerase among the heterogenous intracellular  
448 content seen under electron microscopy<sup>46</sup>. Incorporating the split-APEX2 tag into L and VP35  
449 preserved substantial levels of EBOV polymerase activity, although the valence of intermolecular

450 interaction was increased. This increased valence of intermolecular interactions in VF  
451 components appeared to shift the EBOV VF morphology from the typical droplet-like to network-  
452 like structures, which echoes the network-like VF we observed in EBOV-GFP-ΔVP30 infected  
453 cells. Under such circumstances, we resolved multiple footprints of the EBOV polymerase  
454 gathering at discrete sites in network-like EBOV VFs, where the VF phase boundary was  
455 invaginated or interconnected. These sites may correlate to the EBOV L-foci under confocal light  
456 microscopy.

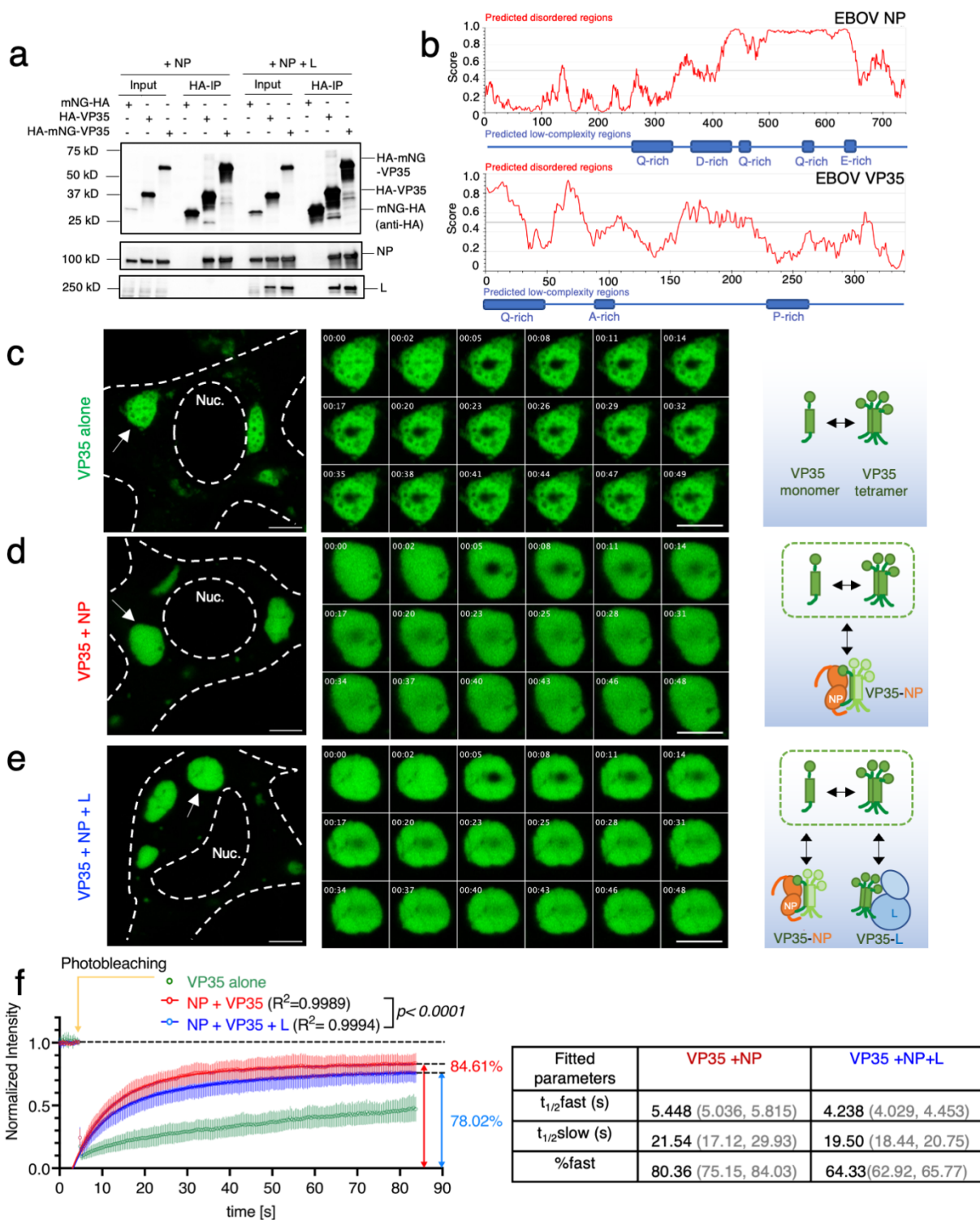
457 Based on our confocal light and electron microscopy findings, we propose a model in which  
458 EBOV polymerase molecules act in concert in a spatially restricted manner. Having a group of  
459 EBOV polymerase molecules acting together on the same viral genome would compensate for  
460 the low efficiency of viral RNA synthesis, as a productive viral RNA synthesis event can only  
461 initiate at a single site at the 3' end of the viral genome<sup>64</sup>. Even so, during transcription, the EBOV  
462 polymerase makes frequent stops at each intergenic region, and at each stop the polymerase  
463 may detach from the genome template. How the same polymerase returns to the 3' end of the  
464 viral genome and initiates a new round of RNA synthesis event is currently unclear. If a group of  
465 EBOV polymerases act on the same viral genome, with some polymerases falling off the template  
466 at certain points, other copies of the polymerase may eventually reach the distal end of the  
467 genome where the L gene is located. By organizing the viral genome in tandem or in another  
468 coordinated way, the same group of polymerases could process more copies of the viral genome  
469 and maximize viral RNA production.

470 This study has several limitations. First, our FRAP analysis is based on the fluorescence  
471 recovery of a sub-area within the VF condensate, which measures a combined rate of molecular  
472 exchange that occur within the VF condensate and occur between the VF and the cytoplasm.  
473 Because the fluorescence intensity of molecules in the VF condensate is ~200-folds higher than  
474 that of the diffused molecules in the cytoplasm and the total VF condensate is significantly larger  
475 than the photo-bleached spot, we reason that the combined rate we measured could approximate  
476 the internal exchange rate within the VF condensate. Indeed, we observed a preferred internal  
477 molecular exchange as in an immediate fluorescence-decay in internal regions within VF that  
478 were not directly photobleached. Nevertheless, FRAP analysis by photobleaching of the full VF  
479 condensate can measure the molecular exchange between the VF condensate and the rest of  
480 the cytoplasm. This measurement is particularly relevant to understand several other stages of  
481 the viral life cycle such as departure of condensed vRNP from VFs as part of viral egress. Second,  
482 the intracellular localization of L we observed either by light or electron microscopy provides an  
483 isolated “snapshot” of only the RNA synthesis stage of EBOV infection. However, EBOV infection  
484 is a continuous process that involves expression of viral matrix proteins (VP24 and VP40) and  
485 viral glycoprotein. The presence of VP24 will change the biological function as well as the physical  
486 properties of EBOV VFs, as the loosely coiled vRNP will be condensed and inevitably reduce the  
487 fluidity of EBOV VF. Meanwhile, viral polymerase will be immobilized in the condensed vRNP and  
488 depart from VFs to the plasma membrane for budding. These virological events are not  
489 recapitulated in the EBOV MG systems used here. Together, the results of our current study  
490 increase our understanding of the mechanisms associated with EBOV VFs and the spatial  
491 regulation of viral RNA synthesis within. Given the similar replication strategy shared among  
492 nNSVs, our findings may be applicable to other critically important nNSV pathogens, such as  
493 rabies, RSV and measles virus.

494

495 **Figures and figure legends**

## Figure 1

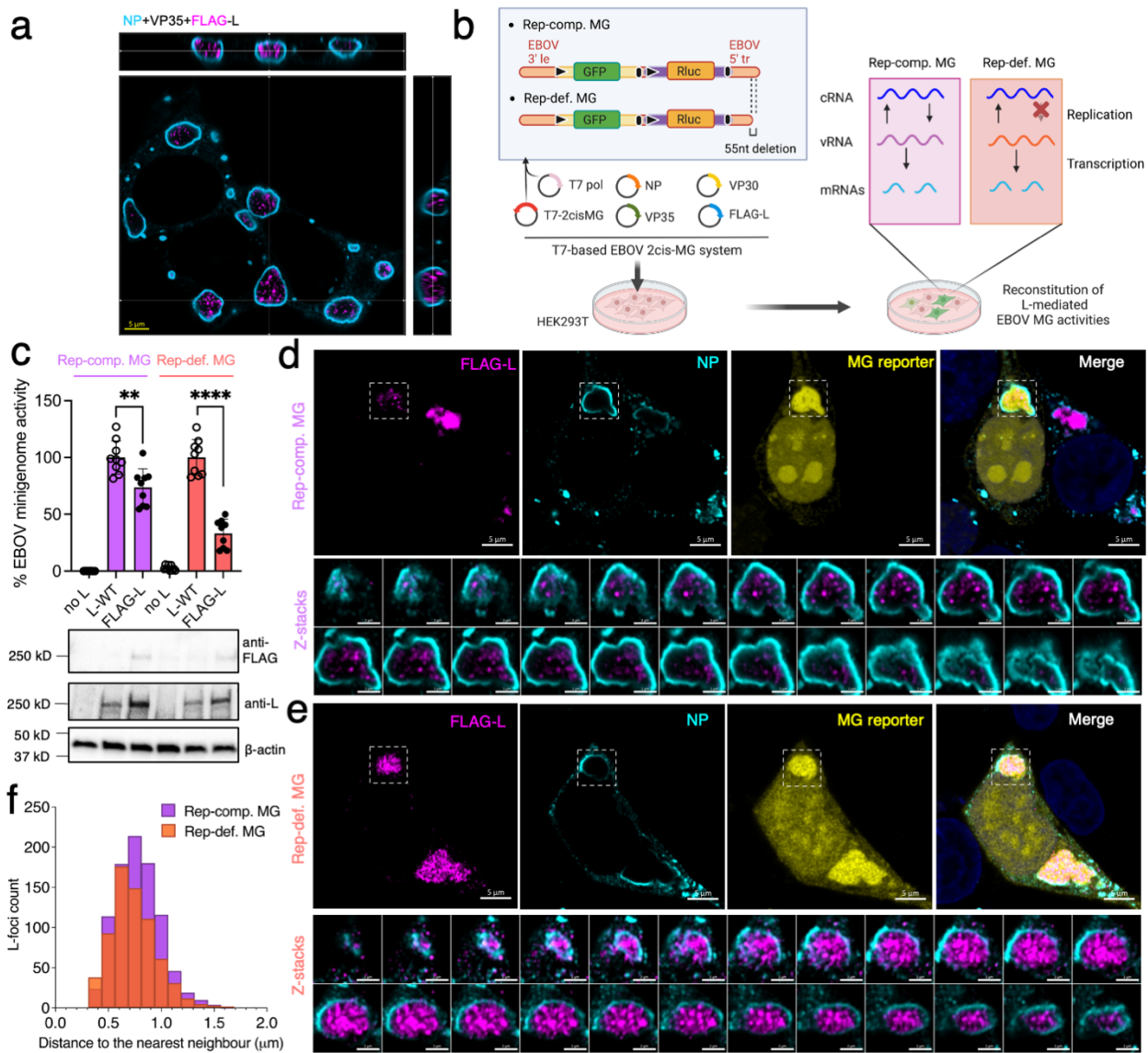


496  
497  
498  
499

**Figure 1. Reconstituted EBOV viral factories with minimal viral protein components display viscoelastic behavior in live cells.** **a** Bioinformatic prediction of intrinsically disordered regions and low complexity regions in the primary sequence of EBOV NP and V35 protein, using the

500 IUPred and PlaToLoCo webserver, respectively. **b** Coimmunoprecipitation (co-IP) of EBOV NP  
501 and L with HA-mNG-VP35. HA-VP35 and HA-mNG served as positive and negative control,  
502 respectively. Anti-HA antibody was used to detect HA-mNG-VP35, HA-VP35, and HA-mNG in the  
503 input cell lysate and in HA-IP fraction. Representative results from 3 biological replicates are  
504 shown. Confocal microscopy of **c** VP35 **d** VP35+NP **e** VP35+NP+L condensates inside live HEK  
505 293T cells 1 d post-transfection. Representative cells (N>6 cells) for each condition from 4  
506 biological replicates are shown. The cell body and nucleus (Nuc.) are marked by a dashed line.  
507 White arrow: individual condensate chosen for photobleaching. Image montage is composed of  
508 selected frames (including t = 0 s) with an interval of 2.88 s from each time-lapse of photobleached  
509 condensate displayed. The diameter of photobleached regions is 1  $\mu\text{m}$ . Photobleaching occurred  
510 at t = 4.8 s. Scale bars: 5  $\mu\text{m}$ . Schematic of EBOV VP35-involved molecular associations  
511 corresponding to each type of condensate. **f** Fluorescence recovery of mNG-HA-VP35 within the  
512 photobleached region inside intracellular condensates containing VP35. Normalized intensity  
513 corresponding to each time point before and after photobleaching of VP35 condensate is shown  
514 in green, VP35+NP condensate is shown in red, VP35+NP+L condensate is shown in blue. Each  
515 data point represents the mean with standard deviation (error bars) of N=9/9/6  
516 (VP35/VP35+NP/VP35+NP+L condensates). Data points with t > 5s in red and in blue were used  
517 to fit a corresponding two-phase association curve, with the normalized intensity value in  
518 expressed as a percentage and the curve plateau marked on the side. Goodness of fit of each  
519 curve is indicated by an  $R^2$  value. An extra sum-of-squares F test was performed to determine  
520 whether the best-fit value for unshared parameters differ between the blue and red curves. For  
521 each fitted curve, the best-fit value for each kinetic parameter is shown with a 95% confidence  
522 interval.  
523

## Figure 2



524

525

**Figure 2. FLAG-tagged EBOV L cluster into foci within reconstituted viral factories. a**

526 Confocal immunofluorescence microscopy of fixed HEK 293T cells co-expressing EBOV NP,

527 VP35 and FLAG-L at 1 d post-transfection. Represented Z-stacks in orthogonal view of 2

528 biological replicates each include > 4 fields of view. Scale bars: 5 μm. **b** Schematics of the T7

529 polymerase (T7 pol), bicistronic EBOV minigenome (2cis-MG) system with a replication

530 competent (Rep-comp.) or replication deficient (Rep-def.) MG. 3' le: 3' leader; 5' tr: 5' trailer; black

531 triangle: gene start; black bar: gene end. **c** Activity of FLAG-L relative to the L-WT control

532 measured in supporting the expression of *Renilla* luciferase (Rluc) in EBOV Rep-comp. vs. Rep-

533 def. MG. Background expression of MG assessed by excluding L in the MG system (no L). Results

534 from 3 biological replicates with technical triplicates are shown as individual data points with mean

535 ± SD (error bars). \*\*,  $p=0.0024$ , \*\*\*\*,  $p<0.0001$  (N=9, two-tailed, unpaired t tests with Welch's

536 correction). Expression of FLAG-L compared to L-WT and detection of the FLAG tag analyzed by

537 western blot using a mouse monoclonal anti-FLAG and a rabbit polyclonal anti-EBOV L antibody,

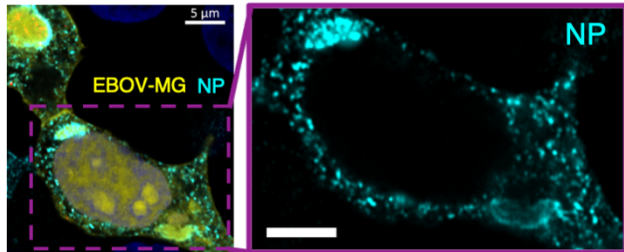
538 respectively. Loading control: β-actin. Confocal microscopy of fixed HEK 293T cells transfected

539 with **d** Rep-comp. or **e** Rep-def. EBOV MG system at 2 d post-transfection. A representative  
540 confocal image overview is shown, in which selected EBOV VFs are marked with a white box  
541 (scale bars: 5  $\mu$ m) and magnified in confocal z-stacks (scale bars: 2  $\mu$ m). Fluorescence of the  
542 GFP reporter in both Rep-comp. and Rep-def. EBOV MG is pseudo-colored in yellow for display  
543 purposes. Nuclei are counterstained with Hoechst. Representative results from 4 biological  
544 replicates with > 5 fields of view are shown. **f** A histogram showing the distribution of nearest  
545 distances between EBOV L-foci within the same VF in the presence of Rep-comp. vs. Rep-def  
546 MG, corresponding to z-stacks shown in (**d**) and (**e**). A total of 908 (Rep-comp.) or 683 (Rep-def.)  
547 L-foci used in quantification.  
548

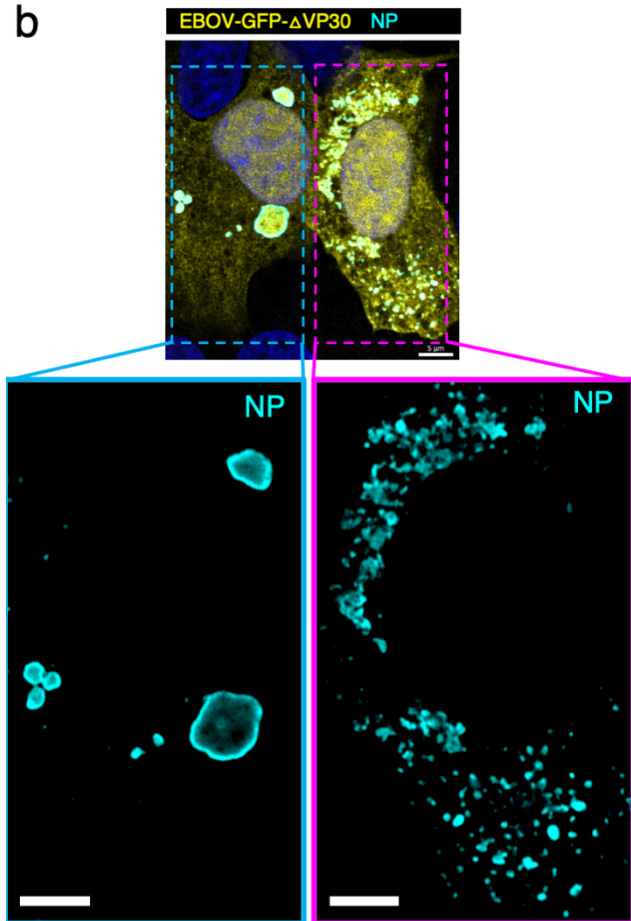
549

## Figure 3

a



b



550

551

552 **Figure 3. Morphologically distinct EBOV viral factories in EBOV minigenome transfected**

553 **cells and EBOV-GFP- $\Delta$ VP30 infected Vero-VP30 cells. a** Confocal immunofluorescence

554 microscopy of HEK 293T cells transfected with T7-pol based, Rep-comp. EBOV MG system, at 2

555 d post transfection. L-WT was used. A representative result from 2 biological replicates with 3

556 fields of view is shown. **b** Confocal immunofluorescence microscopy of representative Vero-VP30

557 cells infected with EBOV-GFP- $\Delta$ VP30 at MOI (multiplicity of infection) = 3, 18 h post infection. A

558 total of N=39 cells from 2 biological replicates were analyzed. In both (a) and (b), fluorescence

559 signals of the GFP reporter in Rep-comp. MG and in EBOV-GFP- $\Delta$ VP30 is pseudo-colored yellow

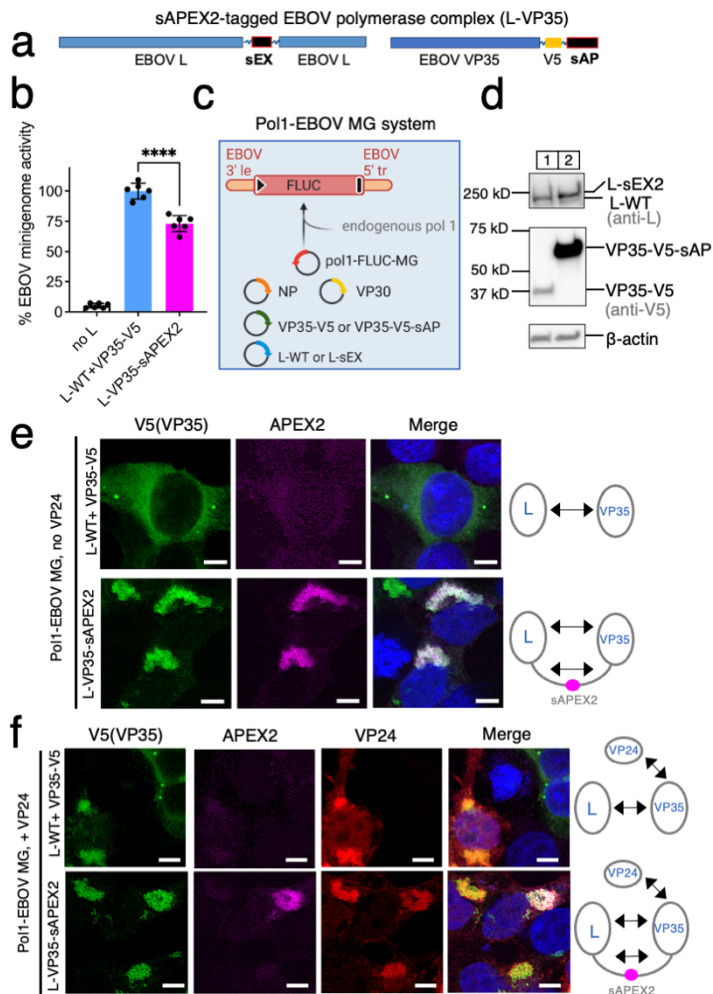
for display purposes. EBOV NP was labeled with a human monoclonal anti-NP antibody paired

560 with Alexa-568 anti-human antibody. The morphologically distinct EBOV viral factory is magnified  
561 in a single channel view. Nucleus counterstained with Hoechst. Scale bars: 5  $\mu$ m.  
562



563

## Figure 4



564

565

**Figure 4. Engineering and characterization of a split-APEX2 tagged EBOV polymerase**

**complex.** **a** Protein constructs of the split-APEX2 (sAPEX2)-tagged EBOV L and VP35. sAPEX

**contains two fragments: sAP and sEX. b** Activity of L-sEX and VP35-V5-sEX (L-VP35-sAPEX2)

**relative to wild-type EBOV L (L-WT) and V5-tagged VP35 (VP35-V5) control measured in**

**supporting expression of firefly luciferase (FLUC) in the EBOV MG. Background expression of**

**MG assessed by excluding L in the MG system (no L). Results from 2 biological replicates with**

**technical triplicates are shown as individual data points with mean ± SD (error bars). \*\*\*\*,**

***p*<0.0001 (N=6, two-tailed, unpaired t tests with Welch's correction). c** Schematic of the RNA

**polymerase 1(Pol1)-based, monocistronic EBOV minigenome system (Pol1-EBOV MG). 3' le: 3'**

**leader; 5' tr: 5' trailer; black triangle: gene start; black bar: gene end. d** Expression of L-sEX

**compared to L-WT and VP35-V5-sAP compared to VP35-V5, each analyzed by western blot**

**using a rabbit polyclonal anti-EBOV L antibody and a mouse monoclonal anti-V5 antibody,**

**respectively. Loading control: β-actin. e** Confocal immunofluorescence microscopy of HEK 293T

**cells transfected with the Pol1-EBOV MG system containing either L-WT +VP35-V5 or L-VP35-**

**sAPEX2, at 2 d post transfection. f** Confocal immunofluorescence microscopy of HEK 293T cells

**transfected with the Pol1-EBOV MG system containing either L-WT +VP35-V5 or L-VP35-**

**sAPEX2, and in the presence of VP24, at 2 d post transfection. In (e) and (f), both VP35-V5-sAP**

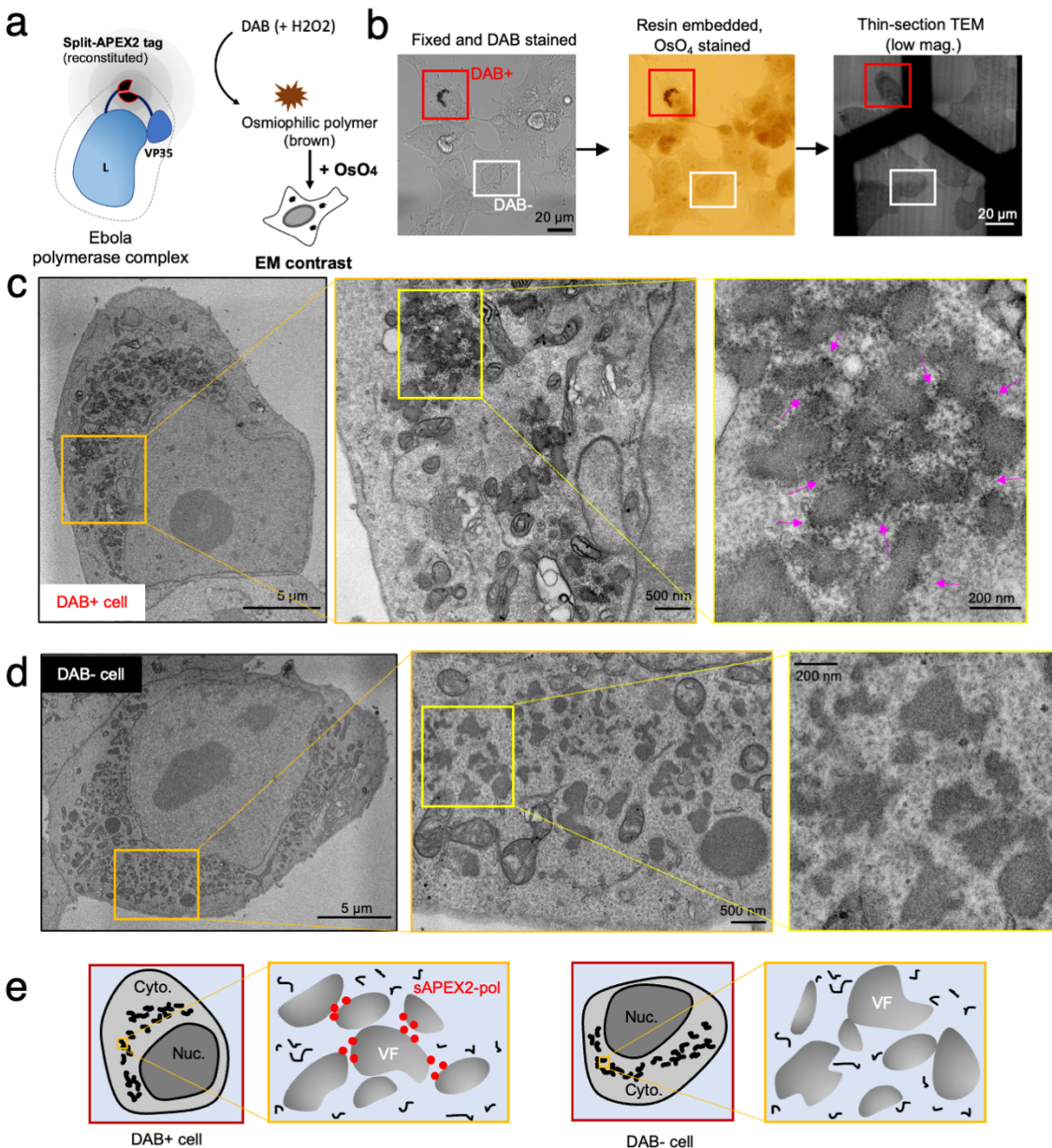
**and VP35-V5 were labeled with a rabbit monoclonal anti-V5 antibody paired with Alexa-488 anti-**

582

583 rabbit antibody. Functional reconstitution of APEX2 was indicated by fluorescence signals from  
584 resorufin, the product of the Amplex UltraRed, a fluorogenic peroxidase substrate for APEX2. In  
585 (f), EBOV VP24 was labeled with a mouse monoclonal anti-VP24 antibody paired with Alexa-488  
586 anti-mouse antibody. Nuclei were counterstained with Hoechst. Fluorescence signals of VP35  
587 and VP24 are pseudo-colored green and red for display purposes. Scale bars: 5  $\mu$ m.  
588 Representative results from 2 biological replicates with >5 fields of view are shown. The valence  
589 of inter-molecular interaction is depicted as double-ended arrows.  
590

591  
592

## Figure 5

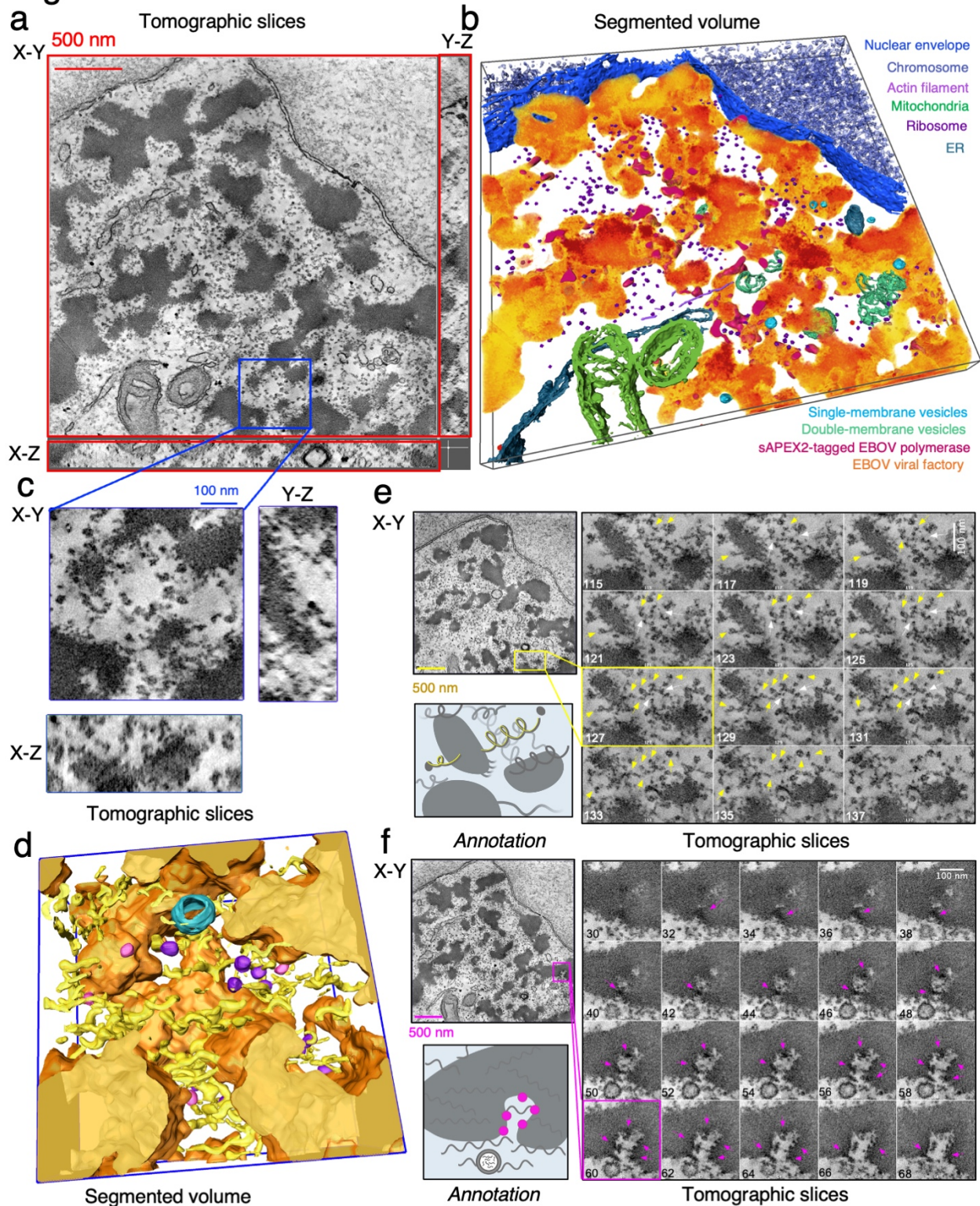


593  
594  
595  
596  
597  
598  
599  
600  
601  
602  
603

**Figure 5 Nanoscale localization of split-APEX2 tagged EBOV polymerase complex revealed by thin-section electron microscopy (EM)** **a** Schematic of the functional reconstitution of APEX2 upon formation of EBOV polymerase (L-VP35) complex and the resulting EM contrast upon DAB-OsO<sub>4</sub> staining. **b** HEK 293T cells were transfected with the Pol1-EBOV-MG system containing sAPEX2-tagged EBOV polymerase (L-VP35) complex and were chemically fixed with 2.5% glutaraldehyde and stained with DAB at 2 d post-transfection. DAB+ and DAB- cells were examined by transmitted light microscopy (left) and then embedded in resin and stained with OsO<sub>4</sub> (middle). The samples were serially sliced into 70 nm-thick sections and imaged with transmission electron microscopy (TEM) at low magnification (right). Scale bars: 20 μm. **c** Electron micrographs of either the overview or a cytoplasmic region of the DAB+ cell indicated in

604 **(b)** at different magnifications. Arrows: sAPEX2 mediated deposition of electron-dense Osmium.  
605 **d** Electron micrographs of either the overview or a cytoplasmic region of the DAB- cell indicated  
606 in **(b)** at different magnifications. Scale bars: 5  $\mu\text{m}$ /500 nm/200 nm in micrographs with a  
607 low/medium/high magnification. **e** Cartoons annotating the whole cell overview, the electron-  
608 dense viral factories (VF) and the sAPEX2-tagged EBOV polymerases (sAPEX2-pol) in both the  
609 magnified DAB+ and DAB- cell, shown in **(c)** and **(d)**, respectively. Representative results from 3  
610 biological replicates with multiple fields of view are shown. Cyto.: cytoplasm. Nuc.: nucleus.  
611

## Figure 6



612  
613  
614  
615

**Figure 6. 3D visualization of EBOV viral factories (VFs) and sAPEX2-tagged polymerase by electron tomography.** a HEK 293 cell transfected with the Pol1-EBOV-MG system containing sAPEX2-tagged EBOV polymerase (L-VP35) complex before fixation with 2.5% glutaraldehyde

616 at 2 d post-transfection. The samples were stained with DAB-OsO<sub>4</sub>, embedded in resin and  
617 sectioned into 250 nm-thick specimens. A reconstructed 3D electron tomogram of the specimen  
618 originating from a DAB+ cell is shown in an orthogonal view with tomographic slices. Scale bar:  
619 500 nm. **B** Segmented volume of the electron-dense EBOV VFs and surface representation of  
620 numerous cellular organelles and sAPEX2-tagged EBOV polymerase, corresponding to the 3D  
621 electron tomogram in (a). **c** Orthogonal view (with X-Y/Y-Z/X-Z plane) showing a magnified  
622 volume of interest in the 3D electron tomogram in (a). Scale bar: 100 nm. **d** Segmented surface  
623 representations of EBOV VFs (orange), sAPEX2-tagged EBOV polymerase (pink), viral RNP coils  
624 (yellow), host ribosomes (purple), and single-membrane vesicle (blue), resulting from the  
625 tomographic volume in (c). **e** Series of magnified tomographic slices on the X-Y plane from a  
626 region containing multiple helical structures that correspond to viral RNPs. Yellow arrows pointing  
627 toward one helical structure; white arrows pointing toward the branch site where multiple helical  
628 structures meet. A cartoon annotation of the same region is shown on the side. **f** A series of  
629 magnified tomographic slices on the X-Y plane from a region containing DAB-osmium deposits  
630 that correspond to sAPEX-tagged EBOV polymerases (indicated by pink arrows) and a single-  
631 membrane vesicle approaching the electron-dense VF. A cartoon annotation of the same region  
632 is shown on the side. For (e) an (f), the scale bar in the tomographic overview slice and magnified  
633 series represents 500 nm and 100 nm, respectively. Tomographic slice number is marked in the  
634 lower left.  
635

## 636 **Methods:**

637 **Plasmids:** If not specified, NEB HiFi assembly was used for incorporation of DNA fragments into  
638 plasmid vector. To generate pCAGGS-mNG-HA-VP35, coding sequence of mNeonGreen (mNG)  
639 was PCR amplified from pmNeonGreenHO-3xFLAG-G (addgene#127914), while an N-terminal  
640 HA epitope tag was added to the mNG coding sequence. The resulting fragment was inserted  
641 upstream of the VP35 coding sequence in pCAGGS-VP35. To generate pCAGGS-HA-VP35  
642 control plasmid, a DNA fragment containing a HA epitope tag followed by a flexible linker was  
643 synthesized and added to the N-terminus of VP35 coding frame. To generate pCMV-mNG-HA  
644 control plasmid, a HA epitope tag was added to the C-terminus of mNG coding sequence. To  
645 generate pCAGGS-VP35-V5-sAP, the fragment of sAP was PCR amplified from  
646 FKBP\_V5\_AP\_NEX\_pLX304 (addgene#120912) and cloned into the intermediate vector  
647 pcDNA5-VP35. The fragment of VP35-V5-sAP was subcloned to pCAGGS plasmid using  
648 restriction sites Xho1 and Nhe1 and standard ligation method. To generate pCAGGS-VP35-V5  
649 control plasmid, the fragment of VP35-V5 was PCR amplified with an addition of a stop codon  
650 and Bgl2 restriction site, and was then incorporated into pCAGGS backbone using Kpn1 and Bgl2  
651 restriction sites.

652 To generate pCAGGS-FLAG-L, a DNA fragment containing a 2xFLAG epitope tag followed  
653 by a flexible linker was synthesized and added to the N-terminus of L coding frame. To generate  
654 pCEZ-L-sEX, a fragment of L coding sequence was first subcloned into a pFastbacDual  
655 intermediate plasmid using the natural restriction sites Pac1 and Hpa1. From there, coding  
656 sequence of sEX was PCR amplified from HA-Halotag-FRB-EX-NES-pLX304 (addgene  
657 #120913), flanked by two flexible linkers and was internally inserted to L fragment at the position  
658 1705/1706 (TTIP/Q). The L-sEX fragment was shuffled back to the pCEZ-L backbone using the  
659 same restriction sites Pac1 and Hpa1.

660 To generate pT7-2cis-MG-Replication competent (Rep-Comp.), the coding sequence of VP40,  
661 GP and VP24, including non-coding sequences VP40/GP and VP30/VP24 in between were  
662 removed from pT7-4cis-EBOV-vRNA-eGFP plasmid<sup>65</sup>, while the coding sequence of *Renilla*  
663 luciferase was inserted downstream of the non-coding sequence NP/VP35 and reassembled. To  
664 generate pT7-2cis-MG-Replication deficient (Rep-def.), the last 55 nucleotide of the 5' trailer  
665 sequence in pT7-2cis-MG-Rep-comp. plasmid was removed by PCR and re-assembled. Other  
666 supporting plasmids used in T7-based EBOV minigenome system were obtained from Dr.  
667 Thomas Hoenen (Friedrich-Loeffler-Institute). Plasmids used in Pol1-based EBOV minigenome  
668 system were obtained from Dr. Yoshihiro Kawaoka (University of Wisconsin Madison).

669 **Cell lines and virus:** Human embryonic kidney cells HEK 293T (ATCC reference: CRL-3216)  
670 were originally purchased from the ATCC organization. Vero cells stably expressing Ebola virus  
671 VP30 protein (Vero-VP30) were obtained from Dr. Yoshihiro Kawaoka (University of Wisconsin  
672 Madison). Both cell lines were maintained in Dulbecco's modified Eagle medium (DMEM-  
673 GlutaMAX) supplemented with 4.5 g/L D-Glucose, 10% fetal bovine serum (FBS), penicillin  
674 (100 U/mL), streptomycin (100 µg/mL). In addition, puromycin (5 µg/mL) was included in the  
675 culture media while maintaining Vero-VP30 cells but excluded for infection experiment. The  
676 biologically contained Ebola virus, EBOV-ΔVP30-GFP was generated in HEK 293T cells and  
677 grown in Vero-VP30 cells as previously described<sup>44</sup>.

678 **Fluorescence Recovery After Photobleaching (FRAP):** IBIDI µ-slides (8 wells high-precision  
679 glass bottom) were treated with human fibronectin (50 mg/mL) for 20 minutes at 37°C incubator,  
680 prior to HEK 293T cells seeding ( $4 \times 10^4$  cells/well). Twenty-four hours later, the monolayer was  
681 transfected with plasmids in three different combinations: 1) 125 ng of pCAGGS-mNG-HA-VP35  
682 and 1 µg of pCAGGS-vector control; 2) 125 ng of pCAGGS-mNG-HA-VP35, 125 ng of pCAGGS-  
683 NP, and 875 ng of pCAGGS-vector control; 3) 125 ng of pCAGGS-mNG-HA-VP35, 125 ng of

684 pCAGGS-NP, and 875 ng of pCAGGS-L (wild-type). Transfected cells were incubated with  
685 complete FluoroBrite DMEM (+1x Glutamax, 10% FBS) for imaging. Time series were acquired  
686 using ZEISS laser scanning microscope (LSM880) with an Airyscan detector while live cells  
687 sample were kept in caged incubator maintaining 37°C and 5% CO<sub>2</sub>. mNG fluorescence was  
688 excited with a 488 nm argon laser and detected with a 63x 1.4NA oil immersion objective (Plan-  
689 Aplanachromat), with a combination of bandpass filters (420-480) and (495-550). Using a frame rate  
690 of 240 millisecond per frame and 0.4% of 488 nm laser, 20 frames were recorded pre-bleach, and  
691 then 330 frames were recorded post-bleach under the Airyscan fast mode. This duration of post-  
692 bleach image acquisition was experimentally determined by the time when fluorescence recovery  
693 reached a plateau. For photobleaching, 488 nm laser at 80% was used to pulse-bleach a spot  
694 size of 1 micron in diameter in the center of large condensates, until the fluorescence intensity of  
695 the bleach spot reduced to 30% of the prebleached value.

696 Time series in which the bleached object moved during post-bleach phase were manually  
697 identified and removed from data analysis because the fluorescence intensity of the bleached  
698 spot could not be accurately measured in ImageJ/FIJI<sup>66</sup>. For each bleach event, double  
699 normalization of the FRAP curve was performed using ImageJ/FIJI as described<sup>15</sup>. To correct  
700 unintentional photobleaching due to time-series acquisition, in every frame, fluorescence intensity  
701 of the bleached spot (1 μm in diameter) was first normalized to the mean intensity of an  
702 unbleached spot (1 μm in diameter) of another condensate in the same field of view. The resulting  
703 values after correction for all frames were further normalized to the average intensity of the last  
704 10 pre-bleach frames. The background intensity in each field of view was negligible as it was  
705 lower than 0.5% of the average intensity of viral factory condensates. Due to biological mobility  
706 of the intracellular condensate and the cellular specimens during imaging, we could not accurately  
707 measure the bleach pulses-induced fluorescence loss in the whole condensate. Instead, we  
708 assessed this parameter in the averaged fluorescence decay of internal reference-regions inside  
709 the same condensate that was photobleached but are away from the bleached spot. Double  
710 normalized data from 6-9 cells in a total of three independent experiments were pooled. Means  
711 with standard deviation of double normalized intensity were plotted as a function of time, of which  
712 post-bleach data-points were fitted to a two-phase association model in GraphPad prism,  
713 according to previously described methods<sup>67</sup>. Best-fit values with 95% confidence interval and  
714 goodness of fit indicated by R<sup>2</sup> for each data set were reported.

$$715 \quad A_{fast} = (Plateau - Y_0) \times \%Fast$$

$$716 \quad A_{slow} = (Plateau - Y_0) \times (1 - \%Fast)$$

$$717 \quad Y(t) = Y_0 + A_{fast}(1 - e^{-k_{fast}t}) + A_{slow}(1 - e^{-k_{slow}t})$$

718 **Immunofluorescence staining and confocal light microscopy:** Fixation and staining was  
719 performed as described<sup>68</sup>.

720 For samples shown in supplementary Figure S1b, human monoclonal anti-Ebola virus NP  
721 (1:2000), mouse monoclonal anti-Ebola virus VP35 (1:500), and rabbit polyclonal anti-Ebola virus  
722 L antibody (1:200) were used as the primary antibodies, goat anti-human Alexa-568 (1:1000),  
723 goat anti-mouse Alexa-647 (1:500), and goat anti-rabbit Alexa-568 (1:500) were used as the  
724 secondary antibodies.

725 For samples shown in Figure 2, human monoclonal anti-Ebola virus NP (1:2000) and mouse  
726 monoclonal anti-FLAG (1:100) antibody were used as the primary antibodies, goat anti-human  
727 Alexa-568 (1:1000) and goat anti-mouse Alexa-647 (1:500) were used as the secondary  
728 antibodies.

729 For samples shown in Figure 3, human monoclonal anti-NP (1:2000) and goat anti-human  
730 Alexa-568 (1:1000) were used.

731 For samples shown in Figure 4, rabbit monoclonal anti-V5 (1:500) and mouse monoclonal  
732 anti-Ebola VP24 (1:1000, a kind gift from Dr. Yoshihiro Kawaoka) were used as the primary



733 antibodies, goat anti-human Alexa-568 (1:1000) and goat anti-mouse Alexa-647 (1:500) were  
734 used as the secondary antibodies. In addition, trans-complemented APEX2 was stained with  
735 Amplex UltraRed at 100 nM (with 0.02% H<sub>2</sub>O<sub>2</sub> in DPBS) on ice for 20 minutes prior to fixation.  
736 Unreacted Amplex UltraRed was washed off with DPBS.

737 Single-plane confocal images or confocal Z-stacks (interval= 0.224 μm) were acquired with  
738 the ZEISS laser scanning microscope (LSM880)-Airyscan system under the superresolution  
739 mode, using a plan-apochromat 20x/0.8 numerical aperture M27 objective or an alpha plan-  
740 apochromat 63x/1.46 numerical aperture oil Korr M27 objective. All images or stacks that are  
741 shown or quantified were Airyscan processed using the Zen black (ZEISS) build-in function.

742 For supplementary Figure 1C, size quantification and counting of reconstituted Ebola viral  
743 factories (VFs) in single-plane confocal images using ImageJ/Fiji. HEK 293T cells were prepared  
744 using identical transfection conditions described in FRAP experiment. VFs were identified on the  
745 basis of mNG-fluorescence and analyzed for the count and size distribution using the analyze  
746 particle function.

747 For Figure 2f, 3D segmentation of Ebola viral factories in confocal Z-stacks was performed in  
748 Imaris 9.9.1 using the surface function and automatically thresholding the GFP intensity;  
749 segmentation of FLAG-tagged Ebola virus L-foci inside each viral factory was performed using  
750 the spot function and automatically thresholding the fluorescence intensity of FLAG-L with an  
751 estimated diameter for each spot as 0.5 μm, which generates specific values of distance to  
752 nearest neighbor for every random pair of segmented spot.

753 **Virus infection with EBOV-GFP-ΔVP30:** Vero-VP30 cells (4X10<sup>4</sup> cells/well) were seeded in  
754 IBIDI μ-slides (8 wells high-precision glass bottom). Twenty-four hours later, the monolayer was  
755 incubated with EBOV-ΔVP30-GFP (MOI=3 foci-forming unit/cell) on ice. After 1 hour, the  
756 monolayer was washed three times with cold DPBS to remove unbound virions and was moved  
757 to the 37°C incubator. Infection was terminated after 16 hours. Infected cells were inactivated with  
758 4% PFA for 15 minutes.

759 **Thin-section TEM with DAB staining:** Sample preparation was adapted from<sup>69</sup>. Mattek 35 mm  
760 dish with NO#1.5 gridded glass bottom (P35G-1.5-14-C-GRD) was treated with human fibronectin  
761 (50 mg/mL) for 1 hour at 37°C incubator, prior to HEK 293T cells seeding (1X10<sup>5</sup> cells/well).  
762 Twenty-four hours later, the monolayer was either untreated or transfected with plasmids in two  
763 different combinations: 1) EBOV Pol1-MG system containing VP35-V5 and L-WT; 2) EBOV Pol1-  
764 MG system containing sAPEX2 tagged L-VP35.

765 For the first combination, 250 ng of pCEZ-NP, 187.5 ng of pCEZ-VP30, 250 ng of pCEZ-  
766 VP35-V5, 156.25 ng of pHH21-3E5E-fluc, and 1875 ng of pCEZ-L were used in the co-  
767 transfection mix for each 35 mm dish. For the second combination, 250 ng of pCEZ-NP, 187.5 ng  
768 of pCEZ-VP30, 250 ng of pCEZ-VP35-V5-sAP, 156.25 ng of pHH21-3E5E-fluc, and 1875 ng of  
769 pCEZ-L-sEX were used in the co-transfection mix for each 35 mm dish.

770 Forty-eight hours post-transfection, cells were fixed first in 2.5% glutaraldehyde-0.1 M  
771 cacodylate buffer pH 7.4 + 2 mM CaCl<sub>2</sub> at room temperature for 1 minute, then fixed in pre-chilled  
772 2.5% glutaraldehyde-0.1 M cacodylate buffer pH 7.4 + 2 mM CaCl<sub>2</sub> on ice for 1 hour, and were  
773 washed three times with cold 0.1 M cacodylate buffer pH 7.4 (cacodylate buffer). Unreacted  
774 fixative in samples was quenched with cold 20 mM Glycine solution for 5 min on ice, followed by  
775 three washes with cold cacodylate buffer. Samples were stained with 2.5 mM DAB (Sigma  
776 #D8001)-0.1 M cacodylate solution in the presence of 1/1000V of 30% H<sub>2</sub>O<sub>2</sub> for 45 minutes on  
777 ice and washed three times with cold cacodylate buffer.

778 Brown DAB stain in samples was confirmed under light microscopy. Samples were then  
779 stained in 1% osmium+1.5% potassium Ferrocyanide in 0.1 M cacodylate buffer on ice for 1 hour  
780 and washed three times with cacodylate buffer. Samples were dehydrated with increasing  
781 concentrations of ethanol (20%, 50%, 70%, 90%, 100%, 100%, 3 minutes each) and washed

782 once in room temperature anhydrous ethanol. Samples were then infiltrated with Durcupan ACM  
783 resin (Electron Microscopy Sciences) using a mixture of anhydrous ethanol: resin (1V:1V) for 30  
784 minutes, then with 100% resin overnight, followed by 48 hours polymerization step at 60 °C.  
785 Ultrathin sections with a 70 nm thickness of embedded specimen were mounted on 200 mesh  
786 hexagonal copper grids with no post-staining step. Electron micrographs were collected using a  
787 FEI Tecnai Spirit transmission electron microscope operating at 120 kV.

788 **Electron tomography and data processing:** Electron tomography was performed using a  
789 300kV Titan Halo equipped with an 8k x 8k direct detector (DE64, Direct Electron). During the  
790 procedure, semi-thick (~250 nm) sections of the resin-embedded specimen were imaged at  
791 different orientations using a 4-tilt acquisition scheme as described<sup>70</sup>, for which the specimen was  
792 tilted from -60 to +60 degrees every 0.25 degree at four different azimuthal orientation. For  
793 aligning the micrographs, 5 nm colloidal gold particles were deposited on each side of the sections  
794 to serve as fiducial markers. The TEM magnification was set at 11,000x, corresponding to a raw  
795 pixel size of 0.36 nm. Tomograms were generated with an iterative reconstruction procedure<sup>70</sup>,  
796 and was binned by a factor of 4 for display and for volume segmentation using Amira 2020 3.1.  
797 software. Membrane organelles were segmented manually combined with automatic thresholding.  
798 Ribosomes were segmented manually. EBOV viral factories and sAPEX2-tagged EBOV  
799 polymerase were segmented with a combination of automatic thresholding and the TopHat tool.

800 **EBOV minigenome assays:** Transfection and activity quantification with Pol1-based  
801 monocistronic EBOV minigenome system was adapted from<sup>47</sup> and described previously<sup>68</sup>.  
802 Transfection with the T7 pol-based EBOV bicistronic minigenome system was adapted from<sup>65</sup>.  
803 Activity of bicistronic minigenome system was measured in *Renilla* luciferase assay. For each  
804 transfection condition, the same cell lysates used in luciferase assay, were pooled from triplicated  
805 assay wells and analyzed in western blot.

806 **Coimmunoprecipitation (coIP):** Co-IP reactions were performed as previously described<sup>68</sup>. HEK  
807 293T cells ( $1 \times 10^6$  cells/well) were seeded in 6-wells plates. Twenty-four hours later, cells in each  
808 well were transfected with 500 ng of pCMV-mNG-HA or pCAGGS-HA-VP35 or pCAGGS-mNG-  
809 HA-VP35 plasmid combined with 500 ng of pCAGGS-NP, with and without 1  $\mu$ g of pCAGGS-L,  
810 using TransIT-LT1 transfection reagent. HA-affinity matrix was used to pull-down protein  
811 complexes containing HA-tagged proteins.

812 **Statistical analysis:** Data shown in Figure 2c, 4a and supplementary Figure 1a were calculated  
813 and plotted in mean with SD. Statistical analysis were analyzed by two-tailed unpaired t-test with  
814 Welch's correction. P values were indicated in figure legends. Data shown in Figure 1f were  
815 analyzed using an extra sum-of-squares F test to compare whether the best-fit values of %Fast,  
816  $k_{fast}$  and  $k_{slow}$  differ between two datasets. The resulting  $p$  value indicating the statistical  
817 significance of the difference was reported in the figure.

818 **Acknowledgments:** We thank Dr. Yoshihiro Kawaoka (University of Wisconsin) for providing the  
819 Pol1-based Ebola minigenome system, sharing the anti-VP30 and anti-VP24 antibodies and the  
820 EBOV-GFP- $\Delta$ VP30 system. We thank Dr. Reika Watanabe (LJI) for providing the EBOV-GFP-  
821  $\Delta$ VP30 virus stock. We thank Dr. Thomas Hoenen (Friedrich-Loeffler-Institute) for sharing the  
822 Ebola tetracistronic trVLP system. We thank Diptiben Parekh (LJI) for plasmid preparations, Dr.  
823 Sharon Schendel (LJI) for manuscript editing, NIH S10OD021831 for sponsoring the Zeiss LSM  
824 880 microscope at the LJI microscopy core facility and an Imaging Scientist grant (2019-198153)  
825 from the Chan Zuckerberg Initiative to S.M. (LJI). We thank NIH R24GM137200 and  
826 S10OD021784 to M.H.E. (UCSD) in support of the National Center for Microscopy and Imaging

827 Research. This research was supported by institutional funds of La Jolla Institute for Immunology  
828 to E.O.S. (LJI). J.F. was supported by the Donald E. and Delia B. Baxter Foundation Fellowship.

829 **Author contributions:** J.F. conceived the study and wrote the paper under the supervision of  
830 E.O.S.; J.F., G.C. and S.M. designed the experiments, J.F., G.C., S.P., S.M., and C.H. performed  
831 the experiments; J.F., G.C., analyzed the data, M.H.E. supervised the data acquisition and  
832 interpretation for electron microscopy analysis, A.A.D. contributed to data interpretation of  
833 intracellular condensates. All authors edited and approved the paper.

834 **References**

835

836 1 Alenquer, M. *et al.* Influenza A virus ribonucleoproteins form liquid organelles at  
837 endoplasmic reticulum exit sites. *Nat Commun* **10**, 1629, doi:10.1038/s41467-019-09549-  
838 4 (2019).

839 2 Cifuentes-Munoz, N., Branttie, J., Slaughter, K. B. & Dutch, R. E. Human Metapneumovirus  
840 Induces Formation of Inclusion Bodies for Efficient Genome Replication and Transcription.  
841 *J Virol* **91**, doi:10.1128/JVI.01282-17 (2017).

842 3 Dolnik, O., Stevermann, L., Kolesnikova, L. & Becker, S. Marburg virus inclusions: A virus-  
843 induced microcompartment and interface to multivesicular bodies and the late  
844 endosomal compartment. *Eur J Cell Biol* **94**, 323-331, doi:10.1016/j.ejcb.2015.05.006  
845 (2015).

846 4 Geiger, F. *et al.* Liquid-liquid phase separation underpins the formation of replication  
847 factories in rotaviruses. *EMBO J* **40**, e107711, doi:10.15252/embj.2021107711 (2021).

848 5 Heinrich, B. S., Cureton, D. K., Rahmeh, A. A. & Whelan, S. P. Protein expression redirects  
849 vesicular stomatitis virus RNA synthesis to cytoplasmic inclusions. *PLoS Pathog* **6**,  
850 e1000958, doi:10.1371/journal.ppat.1000958 (2010).

851 6 Hoenen, T. *et al.* Inclusion bodies are a site of ebolavirus replication. *J Virol* **86**, 11779-  
852 11788, doi:10.1128/JVI.01525-12 (2012).

853 7 Jobe, F., Simpson, J., Hawes, P., Guzman, E. & Bailey, D. Respiratory Syncytial Virus  
854 Sequesters NF-kappaB Subunit p65 to Cytoplasmic Inclusion Bodies To Inhibit Innate  
855 Immune Signaling. *J Virol* **94**, doi:10.1128/JVI.01380-20 (2020).

856 8 Lahaye, X. *et al.* Functional characterization of Negri bodies (NBs) in rabies virus-infected  
857 cells: Evidence that NBs are sites of viral transcription and replication. *J Virol* **83**, 7948-  
858 7958, doi:10.1128/JVI.00554-09 (2009).

859 9 Lee, C. H. *et al.* Reovirus Nonstructural Protein sigmaNS Recruits Viral RNA to Replication  
860 Organelles. *mBio* **12**, e0140821, doi:10.1128/mBio.01408-21 (2021).

861 10 Ringel, M. *et al.* Nipah virus induces two inclusion body populations: Identification of  
862 novel inclusions at the plasma membrane. *PLoS Pathog* **15**, e1007733,  
863 doi:10.1371/journal.ppat.1007733 (2019).

864 11 Zhou, Y., Su, J. M., Samuel, C. E. & Ma, D. Measles Virus Forms Inclusion Bodies with  
865 Properties of Liquid Organelles. *J Virol* **93**, doi:10.1128/JVI.00948-19 (2019).

866 12 Feric, M. *et al.* Coexisting Liquid Phases Underlie Nucleolar Subcompartments. *Cell* **165**,  
867 1686-1697, doi:10.1016/j.cell.2016.04.047 (2016).

868 13 Whelan, S. P., Barr, J. N. & Wertz, G. W. Transcription and replication of nonsegmented  
869 negative-strand RNA viruses. *Curr Top Microbiol Immunol* **283**, 61-119, doi:10.1007/978-  
870 3-662-06099-5\_3 (2004).

871 14 Heinrich, B. S., Maliga, Z., Stein, D. A., Hyman, A. A. & Whelan, S. P. J. Phase Transitions  
872 Drive the Formation of Vesicular Stomatitis Virus Replication Compartments. *mBio* **9**,  
873 doi:10.1128/mBio.02290-17 (2018).

874 15 Nikolic, J. *et al.* Negri bodies are viral factories with properties of liquid organelles. *Nat*  
875 *Commun* **8**, 58, doi:10.1038/s41467-017-00102-9 (2017).

- 876 16 Guseva, S. *et al.* Measles virus nucleo- and phosphoproteins form liquid-like phase-  
877 separated compartments that promote nucleocapsid assembly. *Sci Adv* **6**, eaaz7095,  
878 doi:10.1126/sciadv.aaz7095 (2020).
- 879 17 Boggs, K. B. *et al.* Human Metapneumovirus Phosphoprotein Independently Drives Phase  
880 Separation and Recruits Nucleoprotein to Liquid-Like Bodies. *mBio* **13**, e0109922,  
881 doi:10.1128/mbio.01099-22 (2022).
- 882 18 Risso-Ballester, J. *et al.* A condensate-hardening drug blocks RSV replication in vivo.  
883 *Nature* **595**, 596-599, doi:10.1038/s41586-021-03703-z (2021).
- 884 19 Alberti, S., Gladfelter, A. & Mittag, T. Considerations and Challenges in Studying Liquid-  
885 Liquid Phase Separation and Biomolecular Condensates. *Cell* **176**, 419-434,  
886 doi:10.1016/j.cell.2018.12.035 (2019).
- 887 20 Banani, S. F., Lee, H. O., Hyman, A. A. & Rosen, M. K. Biomolecular condensates: organizers  
888 of cellular biochemistry. *Nat Rev Mol Cell Biol* **18**, 285-298, doi:10.1038/nrm.2017.7  
889 (2017).
- 890 21 Brangwynne, Clifford P., Tompa, P. & Pappu, Rohit V. Polymer physics of intracellular  
891 phase transitions. *Nature Physics* **11**, 899-904, doi:10.1038/nphys3532 (2015).
- 892 22 Ruff, K. M. *et al.* Sequence grammar underlying the unfolding and phase separation of  
893 globular proteins. *Mol Cell* **82**, 3193-3208 e3198, doi:10.1016/j.molcel.2022.06.024  
894 (2022).
- 895 23 Boeynaems, S. *et al.* Spontaneous driving forces give rise to protein-RNA condensates  
896 with coexisting phases and complex material properties. *Proc Natl Acad Sci U S A* **116**,  
897 7889-7898, doi:10.1073/pnas.1821038116 (2019).
- 898 24 Harmon, T. S., Holehouse, A. S., Rosen, M. K. & Pappu, R. V. Intrinsically disordered linkers  
899 determine the interplay between phase separation and gelation in multivalent proteins.  
900 *Elife* **6**, doi:10.7554/eLife.30294 (2017).
- 901 25 Cahn, J. W. & Hilliard, J. E. Free Energy of a Nonuniform System. I. Interfacial Free Energy.  
902 *The Journal of Chemical Physics* **28**, 258-267, doi:10.1063/1.1744102 (1958).
- 903 26 Cahn, J. W. & Hilliard, J. E. Free Energy of a Nonuniform System. III. Nucleation in a Two-  
904 Component Incompressible Fluid. *The Journal of Chemical Physics* **31**, 688-699,  
905 doi:10.1063/1.1730447 (1959).
- 906 27 Hajime, T. Viscoelastic phase separation. *Journal of Physics: Condensed Matter* **12**, R207,  
907 doi:10.1088/0953-8984/12/15/201 (2000).
- 908 28 *Ebola virus disease*, <[https://www.who.int/news-room/fact-sheets/detail/ebola-virus-](https://www.who.int/news-room/fact-sheets/detail/ebola-virus-disease)  
909 [disease](https://www.who.int/news-room/fact-sheets/detail/ebola-virus-disease)> (2022).
- 910 29 *History of Ebola Virus Disease (EVD) Outbreaks*,  
911 <<https://www.cdc.gov/vhf/ebola/history/chronology.html>> (2022).
- 912 30 Kirchdoerfer, R. N., Abelson, D. M., Li, S., Wood, M. R. & Saphire, E. O. Assembly of the  
913 Ebola Virus Nucleoprotein from a Chaperoned VP35 Complex. *Cell Rep* **12**, 140-149,  
914 doi:10.1016/j.celrep.2015.06.003 (2015).
- 915 31 Becker, S., Rinne, C., Hofsass, U., Klenk, H. D. & Muhlberger, E. Interactions of Marburg  
916 virus nucleocapsid proteins. *Virology* **249**, 406-417, doi:10.1006/viro.1998.9328 (1998).
- 917 32 Noda, T., Hagiwara, K., Sagara, H. & Kawaoka, Y. Characterization of the Ebola virus  
918 nucleoprotein-RNA complex. *J Gen Virol* **91**, 1478-1483, doi:10.1099/vir.0.019794-0  
919 (2010).

- 920 33 Shu, T. *et al.* Ebola virus VP35 has novel NTPase and helicase-like activities. *Nucleic Acids*  
921 *Res* **47**, 5837-5851, doi:10.1093/nar/gkz340 (2019).
- 922 34 Watanabe, S., Noda, T. & Kawaoka, Y. Functional mapping of the nucleoprotein of Ebola  
923 virus. *J Virol* **80**, 3743-3751, doi:10.1128/JVI.80.8.3743-3751.2006 (2006).
- 924 35 Bruhn, J. F. *et al.* Crystal Structure of the Marburg Virus VP35 Oligomerization Domain. *J*  
925 *Virol* **91**, doi:10.1128/JVI.01085-16 (2017).
- 926 36 Chanthamontri, C. K. *et al.* The Ebola Viral Protein 35 N-Terminus Is a Parallel Tetramer.  
927 *Biochemistry* **58**, 657-664, doi:10.1021/acs.biochem.8b01154 (2019).
- 928 37 Zinzula, L. *et al.* Structures of Ebola and Reston Virus VP35 Oligomerization Domains and  
929 Comparative Biophysical Characterization in All Ebolavirus Species. *Structure* **27**, 39-54  
930 e36, doi:10.1016/j.str.2018.09.009 (2019).
- 931 38 Sprague, B. L. & McNally, J. G. FRAP analysis of binding: proper and fitting. *Trends Cell Biol*  
932 **15**, 84-91, doi:10.1016/j.tcb.2004.12.001 (2005).
- 933 39 Trunschke, M. *et al.* The L-VP35 and L-L interaction domains reside in the amino terminus  
934 of the Ebola virus L protein and are potential targets for antivirals. *Virology* **441**, 135-145,  
935 doi:10.1016/j.virol.2013.03.013 (2013).
- 936 40 Nelson, E. V. *et al.* Ebola Virus Does Not Induce Stress Granule Formation during Infection  
937 and Sequesters Stress Granule Proteins within Viral Inclusions. *J Virol* **90**, 7268-7284,  
938 doi:10.1128/JVI.00459-16 (2016).
- 939 41 Zhu, L. *et al.* Ebola virus VP35 hijacks the PKA-CREB1 pathway for replication and  
940 pathogenesis by AKIP1 association. *Nat Commun* **13**, 2256, doi:10.1038/s41467-022-  
941 29948-4 (2022).
- 942 42 Muhlberger, E., Weik, M., Volchkov, V. E., Klenk, H. D. & Becker, S. Comparison of the  
943 transcription and replication strategies of marburg virus and Ebola virus by using artificial  
944 replication systems. *J Virol* **73**, 2333-2342, doi:10.1128/JVI.73.3.2333-2342.1999 (1999).
- 945 43 Hoenen, T., Jung, S., Herwig, A., Groseth, A. & Becker, S. Both matrix proteins of Ebola  
946 virus contribute to the regulation of viral genome replication and transcription. *Virology*  
947 **403**, 56-66, doi:10.1016/j.virol.2010.04.002 (2010).
- 948 44 Halfmann, P. *et al.* Generation of biologically contained Ebola viruses. *Proc Natl Acad Sci*  
949 *U S A* **105**, 1129-1133, doi:10.1073/pnas.0708057105 (2008).
- 950 45 Nanbo, A., Watanabe, S., Halfmann, P. & Kawaoka, Y. The spatio-temporal distribution  
951 dynamics of Ebola virus proteins and RNA in infected cells. *Sci Rep* **3**, 1206,  
952 doi:10.1038/srep01206 (2013).
- 953 46 Han, Y. *et al.* Directed Evolution of Split APEX2 Peroxidase. *ACS Chem Biol* **14**, 619-635,  
954 doi:10.1021/acscchembio.8b00919 (2019).
- 955 47 Jasenosky, L. D., Neumann, G. & Kawaoka, Y. Minigenome-based reporter system suitable  
956 for high-throughput screening of compounds able to inhibit Ebolavirus replication and/or  
957 transcription. *Antimicrob Agents Chemother* **54**, 3007-3010, doi:10.1128/AAC.00138-10  
958 (2010).
- 959 48 Schmelzer, J. W., Abyzov, A. S. & Moller, J. Nucleation versus spinodal decomposition in  
960 phase formation processes in multicomponent solutions. *J Chem Phys* **121**, 6900-6917,  
961 doi:10.1063/1.1786914 (2004).
- 962 49 Tanaka, H. Viscoelastic phase separation in biological cells. *Communications Physics* **5**, 167,  
963 doi:10.1038/s42005-022-00947-7 (2022).

- 964 50 Banadyga, L. *et al.* Ebola virus VP24 interacts with NP to facilitate nucleocapsid assembly  
965 and genome packaging. *Sci Rep* **7**, 7698, doi:10.1038/s41598-017-08167-8 (2017).
- 966 51 Wigglesworth, V. B. The use of osmium in the fixation and staining of tissues. *Proceedings*  
967 *of the Royal Society of London. Series B - Biological Sciences* **147**, 185-199,  
968 doi:10.1098/rspb.1957.0043 (1957).
- 969 52 Neidle, S. & Stuart, D. I. The crystal and molecular structure of an osmium bispyridine  
970 adduct of thymine. *Biochim Biophys Acta* **418**, 226-231, doi:10.1016/0005-  
971 2787(76)90072-1 (1976).
- 972 53 Zhang, J., Li, D., Zhang, J., Chen, D. & Murchie, A. I. Osmium tetroxide as a probe of RNA  
973 structure. *RNA* **23**, 483-492, doi:10.1261/rna.057539.116 (2017).
- 974 54 Geisbert, T. W. & Jahrling, P. B. Differentiation of filoviruses by electron microscopy. *Virus*  
975 *Res* **39**, 129-150, doi:10.1016/0168-1702(95)00080-1 (1995).
- 976 55 Beniac, D. R. *et al.* The organisation of Ebola virus reveals a capacity for extensive,  
977 modular polyploidy. *PLoS One* **7**, e29608, doi:10.1371/journal.pone.0029608 (2012).
- 978 56 Bharat, T. A. *et al.* Structural dissection of Ebola virus and its assembly determinants using  
979 cryo-electron tomography. *Proc Natl Acad Sci U S A* **109**, 4275-4280,  
980 doi:10.1073/pnas.1120453109 (2012).
- 981 57 Watanabe, S., Noda, T., Halfmann, P., Jasenosky, L. & Kawaoka, Y. Ebola virus (EBOV) VP24  
982 inhibits transcription and replication of the EBOV genome. *J Infect Dis* **196 Suppl 2**, S284-  
983 290, doi:10.1086/520582 (2007).
- 984 58 Watt, A. *et al.* A novel life cycle modeling system for Ebola virus shows a genome length-  
985 dependent role of VP24 in virus infectivity. *J Virol* **88**, 10511-10524,  
986 doi:10.1128/JVI.01272-14 (2014).
- 987 59 Bodmer, B. S. & Hoenen, T. Assessment of Life Cycle Modeling Systems as Prediction Tools  
988 for a Possible Attenuation of Recombinant Ebola Viruses. *Viruses* **14**,  
989 doi:10.3390/v14051044 (2022).
- 990 60 Blanchard, E. L. *et al.* Polymerase-tagged respiratory syncytial virus reveals a dynamic  
991 rearrangement of the ribonucleocapsid complex during infection. *PLoS Pathog* **16**,  
992 e1008987, doi:10.1371/journal.ppat.1008987 (2020).
- 993 61 Nilsson-Payant, B. E. *et al.* Reduced Nucleoprotein Availability Impairs Negative-Sense  
994 RNA Virus Replication and Promotes Host Recognition. *J Virol* **95**, doi:10.1128/JVI.02274-  
995 20 (2021).
- 996 62 Hu, Z. *et al.* Inclusion bodies of human parainfluenza virus type 3 inhibit antiviral stress  
997 granule formation by shielding viral RNAs. *PLoS Pathog* **14**, e1006948,  
998 doi:10.1371/journal.ppat.1006948 (2018).
- 999 63 Ma, W., Zheng, G., Xie, W. & Mayr, C. In vivo reconstitution finds multivalent RNA-RNA  
1000 interactions as drivers of mesh-like condensates. *eLife* **10**, e64252,  
1001 doi:10.7554/eLife.64252 (2021).
- 1002 64 Deflube, L. R. *et al.* Ebolavirus polymerase uses an unconventional genome replication  
1003 mechanism. *Proc Natl Acad Sci U S A* **116**, 8535-8543, doi:10.1073/pnas.1815745116  
1004 (2019).
- 1005 65 Schmidt, M. L., Tews, B. A., Groseth, A. & Hoenen, T. Generation and Optimization of a  
1006 Green Fluorescent Protein-Expressing Transcription and Replication-Competent Virus-

- 1007 Like Particle System for Ebola Virus. *J Infect Dis* **218**, S360-S364, doi:10.1093/infdis/jiy405  
1008 (2018).
- 1009 66 Schindelin, J. *et al.* Fiji: an open-source platform for biological-image analysis. *Nat*  
1010 *Methods* **9**, 676-682, doi:10.1038/nmeth.2019 (2012).
- 1011 67 Taylor, N. O., Wei, M.-T., Stone, H. A. & Brangwynne, C. P. Quantifying Dynamics in Phase-  
1012 Separated Condensates Using Fluorescence Recovery after Photobleaching. *Biophysical*  
1013 *Journal* **117**, 1285-1300, doi:<https://doi.org/10.1016/j.bpj.2019.08.030> (2019).
- 1014 68 Fang, J. *et al.* Functional interactomes of the Ebola virus polymerase identified by  
1015 proximity proteomics in the context of viral replication. *Cell Rep* **38**, 110544,  
1016 doi:10.1016/j.celrep.2022.110544 (2022).
- 1017 69 Martell, J. D., Deerinck, T. J., Lam, S. S., Ellisman, M. H. & Ting, A. Y. Electron microscopy  
1018 using the genetically encoded APEX2 tag in cultured mammalian cells. *Nat Protoc* **12**,  
1019 1792-1816, doi:10.1038/nprot.2017.065 (2017).
- 1020 70 Phan, S. *et al.* 3D reconstruction of biological structures: automated procedures for  
1021 alignment and reconstruction of multiple tilt series in electron tomography. *Adv Struct*  
1022 *Chem Imaging* **2**, 8, doi:10.1186/s40679-016-0021-2 (2017).  
1023